Silicon isotopic re-equilibration during amorphous silica precipitation and implications for isotopic signatures in geochemical proxies

Nicole M. Fernandez, Xu Zhang, Jennifer L. Druhan

Version of Record: https://www.sciencedirect.com/science/article/pii/S0016703719304533
Manuscript_9e74392d29a3e7697e0caf1b0154c72c

Silicon isotopic re-equilibration during amorphous silica precipitation and implications for isotopic signatures in geochemical proxies

Nicole M. Fernandez[1,2*], Xu Zhang[2], Jennifer L. Druhan[1]

1. Department of Geology, University of Illinois at Urbana-Champaign Urbana, Illinois 61801 USA

2. Université de Paris, Institut de physique du globe de Paris, CNRS, F-75005 Paris, France

Corresponding author email: frnndzf2@illinois.edu

ABSTRACT

Water-rock interactions influence the isotopic signatures archived during secondary mineral formation and thus the fidelity with which these geochemical proxies retain pristine geochemical records over geologic timescales. The extent to which these isotopic signatures are "re-equilibrated" or "reset" has been suggested to be dependent on surface area and the depth into mineral surface that the surrounding fluid can access, but this relationship has yet to be incorporated in a generalized modeling framework. In this study, we evaluate the timing and extent of silicon isotopic re-equilibration during amorphous silica formation, a common secondary mineral in weathering environments, through a combination of both laboratory experiments and multi-component numerical modeling. A series of amorphous silica precipitation experiments were conducted over a range of surface areas and solid to fluid ratios at 20°C and near neutral pH for a period of 30 days. These experiments show evidence that surface area exerts a first order control on the extent of isotopic re-equilibration following secondary mineral precipitation. New mineral growth onto higher surface areas seeds resulted in rapid isotopic re-equilibration (over a period of ~2 weeks) whereas precipitation onto lower surface area grains retained a kinetic signature due to overall slower kinetics. Experimental results were further supported by a modified numerical reaction network model that has the novel capacity to explicitly treat the depth into the mineral that the fluid can chemically and

isotopically exchange with through time. These numerical simulations demonstrate that the fluid-mineral surface interaction depth is larger for low surface area seed crystals where both a larger mass of amorphous silica was formed, and slower precipitations rates kept the reaction far from equilibrium, thereby impeding the influence of the back reaction and corresponding isotopic re-equilibration. These results highlight the significant role that water-rock interaction and, specifically, the mineral surface plays in the preservation of isotopic signatures within secondary silicate phases. Further, we suggest that a transient model approach is necessary to improve quantitative interpretations of observed isotope behavior in natural systems.

1. INTRODUCTION

Secondary minerals are a critical geochemical archive of Earth's development and evolution throughout geologic time up to the modern day. Their chemical and isotopic compositions provide a snapshot of the (paleo)environmental conditions under which they formed. In modern terrestrial settings, these geochemical proxies can be used to elucidate geochemical and hydrological processes regulating global geochemical cycling of solutes that govern Earth's climate and ecosystems. Rapid analytical advancements over the past several decades have allowed for stable isotopes of many elements found as either major (Si, Mg, Ca, Fe) or minor (Li, Sr, B) constituents of minerals to be measured with high precision. These mass-dependent tracers have become powerful tools for extracting the wealth of information preserved within secondary minerals. The high sensitivity of non-traditional stable isotopes to water-mineral interactions and characteristic fractionations associated with the precipitation of individual secondary phases (quantified through a fractionation factor, α) has made them exceptionally useful. One important application of these stable isotopes is in the quantification of weathering rates where primary mineral solubilization and secondary

mineral formation pathways are highly coupled (Maher et al., 2006; Maher et al., 2009; Zhu and Lu, 2009) and, thus, hard to tease apart solely through dissolved solute concentrations. As a consequence, stable isotopes are frequently used to characterize precipitation weathering reactions ranging from secondary carbonate (Tipper et al., 2006; Lemarchand and Gaillardet, 2006; Tipper et al., 2008; Jacobson et al., 2015, and others) to silicate phases (Georg et al., 2006; Georg et al., 2007; Pogge von Strandmann et al., 2008; Pokrovsky et al., 2013; Geilert et al., 2015; Steinhoefel et al., 2017, and others).

Despite substantial progress, quantitative analysis of secondary mineral formation and their associated stable isotope signatures are still limited by a fundamental knowledge gap in both the establishment of a growing mineral's isotopic composition and how it evolves through time and space. This ambiguity in the processes contributing to observed isotope ratios have led to questions regarding the fidelity of geochemical proxies and the preservation of isotopic signatures imparted during mineral growth over long periods of time (Fantle and DePaolo, 2007; Fantle, 2010; Fantle, 2015; Huber et al., 2017; Gorski and Fantle, 2017). Several studies suggest that alterations to stable isotope records can occur rapidly even in low temperature environments and systems that operate close to equilibrium (Handler et al., 2009; Curti et al., 2010, and others). Evidence for such "isotopic re-equilibration" is largely found in the carbonate literature, but this behavior has also been observed in other secondary phases such as Fe oxides (Frierdich et al., 2014; Handler et al., 2014; Frierdich et al., 2015; Joshi et al., 2017) and silicates (Geilert et al., 2014; Oelze et al., 2014; Roerdink et al., 2015). Studies focusing on a variety of crystalline carbonates have shown isotopic re-equilibration to occur rapidly, on the order of weeks (Mavromatis et al., 2012; Pearce et al., 2012; Mavromatis et al., 2015; Mavromatis et al., 2016; Mavromatis et al., 2017; Oelkers et al., 2018). Notably, recent observations for $\delta^{30}Si$ fractionation during amorphous silica precipitation in both the field (Frings et al., 2016) and laboratory (Geilert et al., 2014; Roerdink et al., 2015; Oelze et

al., 2015) suggest comparable timescales of isotopic re-equilibration can occur during silicate mineral formation in low temperature environments. Isotopic re-equilibration in secondary phases such as amorphous silica, which represents an important ^{30}Si-depleted terrestrial reservoir (Basile-Doelsch et al., 2005) and an increasingly employed geochemical proxy for modern weathering environments (Georg et al., 2007; Georg et al., 2009; Oelze et al., 2014; Tatzel et al., 2015; Alfredsson et al., 2015; Steinhoefel et al., 2017, and others), implies that even isotopic signatures of slow forming secondary minerals can be significantly altered on relatively short timescales (< 1 Ma). As secondary minerals include a wide variety of crystal structures with different metal contents, solubilities and stabilities, identifying the mechanisms underlying stable isotope fractionation during the complete lifespan of formation and residence in the environment is critical and serves as the principle motivation for this study.

How then does isotopic "re-equilibration" occur and what controls its timing and extent? Isotopic re-equilibration takes place after the kinetically dominant portion of a reversible reaction has ceased and overall rates have slowed down in the approach to a dynamic equilibrium (i.e. when the forward, precipitation rate and backward, dissolution rate equal one another). As this dynamic equilibrium is initially established, the distribution of isotope ratios between phases can remain at far-from-equilibrium conditions and, thus, continue to exchange between the mineral surface and the surrounding fluid. As a result, kinetic signatures generated during precipitation begin to be "erased" through increasing contributions from equilibrium fractionation until isotopic equilibrium is established. Consequences of this dynamic interplay between kinetic and equilibrium isotope effects imply that application of traditional kinetic (Rayleigh, 1902; Hofmann et al., 2012) or equilibrium (Méheut et al., 2007; Schauble et al., 2009; Méheut and Schauble, 2014; Dupuis et al., 2015; He et al., 2015) isotope fractionation models characterized by fixed fractionation

factors (α_{kin} and α_{eq}), while viable in certain situations, would fail to fully capture the variable isotopic behavior readily observed in the α of many natural environments (Bouchez et al., 2013).

To address this limitation in conventional stable isotope fractionation frameworks, DePaolo (2011) developed a steady-state model based on dynamic equilibrium and surface exchange reactions to better describe observed variability in isotope partitioning. In the surface reaction kinetic model, isotopic re-equilibration is manifested in a variable observed fractionation factor (α_{obs}) that is influence by the relative contributions of both kinetic (α_{kin}) and equilibrium (α_{eq}) isotope fractionation and varies as a function of precipitation rate. Recent application of the surface reaction kinetic model to quantify observed $\delta^{30}Si$ fractionation between aqueous and amorphous silica in the Geilert et al.(2014) flow through and Roerdink et al.(2015) batch precipitation experiments supports the conceptual framework put forth by DePaolo (2011) to characterize isotopic re-equilibration in low temperature settings. However, assumptions that form the basis of the original DePaolo (2011) model limit its direct application to natural systems. Specifically, the underlying assumption of chemostatic conditions (where solute compositions and saturations are fixed) results in a condition where the growing mineral surface in contact with the fluid maintains a steady state isotope composition. While this steady state approach is reasonable under highly controlled precipitation experiments, it may be insufficient to predict observed fractionation factors in transient settings where saturation states are highly variable. Thus, we suggest an expanded treatment of observed stable isotope fractionation behavior may be gained by modifying this mixed kinetic and equilibrium partitioning to incorporate a transient framework for fluid-mineral interactions during secondary mineral formation.

A transient numerical framework for combined kinetic and equilibrium isotope effects in open systems was developed by Druhan et al. (2013) using a solid solution capable of

producing the same behavior as the DePaolo (2011) derivation for a coupled, co-evolving fluid and solid mineral. In this approach, the isotopic evolution between the fluid and growing mineral is dependent on the evolving isotope ratio of the mineral in communication with the fluid phase. An important parameter that arises in this transient schematic is the amount of overall mineral available for re-equilibration with the fluid. Thus, the approach offers a framework to couple observable fluid isotopic exchange to the subcomponent of the mineral mass that is in communication with the surrounding fluid, i.e. the depth into the mineral surface that the fluid can interact with. A key prediction that arises from this transient-based model is that *the rate and extent of isotopic re-equilibration during fluid-mineral interactions must be dependent on the mineral surface area* (Druhan et al., 2013; Druhan and Brown, 2015). The influence of surface area on reaction rates in water-rock interactions has been well established in the literature (Aagaard and Helgeson, 1982; Helgeson et al., 1984; Holdren and Speyer, 1985; Murphy et al., 1989), but, to date, the role that the surface area plays on (paleo)environmental isotopic signatures has yet to be explored in such a forward modeling framework. Here, we address the extent to which variations in surface area influence the observed fractionation factor between co-evolving fluid and newly formed solids through a series of amorphous silica precipitation experiments conducted under conditions resembling natural, open systems. We then compare these results with a series of transient numerical CrunchTope models using a variety of approximations for the fluid-mineral surface interaction depth. This study is highly relevant to natural weathering environments in which amorphous silica is a common secondary product, and more generally addresses the extent to which stable isotope fractionation (1) exhibits a surface area dependence and (2) persists through time.

2. METHODS

2.1 Experimental methods

153 Amorphous silica precipitation was conducted in stirred batch reactors using known
154 weights of $SiO_{2(am)}$ seed crystals over a range of initial surface areas and solid:fluid mass
155 ratios. The experiments were subjected to conditions where the saturation state is variable (i.e.
156 allowed to change throughout the course of the experiment) for a timespan of approximately
157 thirty days (Nancollas and Reddy, 1971; Wiechers et al., 1975; Inskeep and Bloom, 1985;
158 Zhang and Dawe, 1998). Starting conditions are succinctly summarized in **Table 1**. Silica
159 seed crystals of three distinct grain sizes and BET (Brunauer-Emett-Teller) defined specific
160 surface areas (SSA, m^2/g) were utilized for the experiments. The silica seeds used in the high
161 SA ("surface area") batch were a hydrophilic fumed high-purity silica powder with a BET
162 constrained surface area of 50 m^2/g (AEROSIL® OX50). The medium and low SA batches
163 consisted of high purity silica flours with BET constrained surface areas analyzed by
164 AGSCO® company of 0.127 m^2/g (AGSCO® SILICA FLOUR 325) and 0.072 m^2/g
165 (AGSCO® SILICA FLOUR 200). The batch experiments followed procedures adapted from
166 Roerdink et al. (2015) and Geilert et al. (2014). Amorphous silica precipitation occurred
167 heterogeneously (i.e. fumed silica or silica flour was initially present in the reactor) and solid
168 to fluid mass ratios for the experiments using the high surface area and the medium/low
169 surface area grains were 32 $gSiO_{2(s)}$:$gSiO_{2(aq)}$ and 50 $gSiO_{2(s)}$:$gSiO_{2(aq)}$, respectively. An
170 initially supersaturated solution with respect to amorphous silica was prepared by first
171 dissolving 10 g L^{-1} of the AEROSIL® OX50 fumed silica particles in ultra-pure water
172 (18.2mΩ) in a fluorinated ethylene propylene (FEP) bottle at a temperature of 90℃ for ~ 7-10
173 days, allowing the solution to attain a solubility concentration in the range of 320-330 ppm
174 SiO_2 (Gunnarsson and Anórsson, 2000). These concentrations are higher than average
175 dissolved SiO_2 in natural waters (~9.61 ppm, Dürr et al., 2011), but traditionally amorphous
176 silica precipitation experiments are run at elevated values to speed up an otherwise
177 infamously slow reaction (Iler, 1979; Fleming, 1986). To initiate precipitation, the 90℃

starting silica solution were divided into multiple HDPE batch reactors. For the high SA (50 $m^2 g^{-1}$) experiment, the 50 mL batch reactor was cooled down for ~ 30 min in a water bath to the targeted temperature of 20℃ with the remaining undissolved fumed silica crystals serving as the nucleation seeds. For the medium (0.127 $m^2 g^{-1}$) and low (0.072 $m^2 g^{-1}$) SA experiments, vacuum filtration was performed using a Merck Millipore 0.20 µm filter and then distributed into 250 mL HDPE reactor vessels that were cooled down to 20℃. Once at the targeted temperature, the initially low pH (~4.3) solutions were brought up to near neutral pH (~7.3) through the addition of 10mM NaOH solution. Precipitation in the high SA experiment was initiated immediately following the alkalization procedure. Medium and low SA experiments were initialized following the combination of alkalization and immediate addition of 4.0 g of the respective silica flours. The solutions were continuously agitated throughout the duration of the experiments on a shaker plate to ensure homogeneity and to avoid transport (diffusive) boundary layer effects between the bulk fluid and amorphous silica surfaces. Fluid samples were taken from each batch reactor at the beginning of the precipitation experiments (t = 0) and at regular time intervals in aliquots of 2.5 mL using a disposable syringe. Samples were filtered through 0.22 µm nylon membrane syringe filters and solid amorphous silica precipitates were collected at the end of the experiment via vacuum filtration using Merck Millipore 0.22 µm filters and dried at room temperature.

2.2 Analytical methods

Silica concentrations were quantified using 0.5 mL aliquots of the filtered samples diluted to 10 mL with ultrapure water and acidified with 2% HNO_3. The fluid phase silicon concentrations were then analyzed using an Agilent 7900 Inductively Coupled Plasma Mass Spectrometer at the Ínstitut de Physique du Globe de Paris (IPGP) in Paris, France. Instrumental precision using a multi-element standard for Si (based on the abundant isotope Si-28) and an internal standard using Sc for correction due to matrix effects was ±0.06 mM

(1RSD). Although only the total dissolved silicon concentrations were determined in this study, we based our procedure on prior work demonstrating that only minor polymerization occurred during precipitation and the difference between total dissolved silica and monomeric SiO_2 falls below 10% (Geilert et al., 2014; Roerdink et al., 2015). Fluid stable isotope sample preparation began by diluting 2 mL of each filtered aliquot to a targeted volume of 10 mL with ultrapure water. Precipitated amorphous silica samples were collected via vacuum filtration through a Merck Millipore 0.22 μm filter and prepared for isotopic analysis following digestion by an adapted Alkali fusion technique (Georg et al., 2006) where 20 mg of solid sample was combined with 200 mg of analytical grade NaOH and fluxed in Ag crucibles heated to 720℃ for 12 min in a muffle furnace. The resulting product was then allowed to dissolve in PTFE vials containing 15 mL of ultrapure water for 24 hours followed by acidification with twice-distilled concentrated HNO_3 to a target 2% HNO_3 concentration.

Following these preparation procedures both fluid and solid phase samples were subjected to the same column chemistry modified from Van Den Boorn et al. (2006), Georg et al. (2006b), and Pringle et al. (2014) using a BioRad AG50W-X12 cation-exchange resin for sample purification. Silicon purification involved adding 20 μg Si as an acidified fluid sample to pre-cleaned 1.8mL resin bed in BioRad columns and eluted via addition of 5 mL MQ-e water. Silicon yields were approximately 70% for the first elution step (2 mL MQ-e) and the remaining 30% was recovered in the final elution step (3 mL MQ-e). Procedural blanks run through this column chemistry had ^{28}Si signals indistinguishable from the ^{28}Si blank on the mass spectrometer (~ 20 mV corresponding to less than 1% of the ^{28}Si sample signal). Silicon isotopic analyses were performed on a ThermoFinnigan Neptune Plus MC-ICP-MS at the Institut de Physique du Globe de Paris. Running conditions on the machine closely follow the method established by Georg et al. (2006). Samples were introduced as a wet plasma using a classic stable introduction system (SIS: double Scott/cyclonic spray chamber) and a 100 μL

228 min^{-1} Teflon® nebulizer. To separate polyatomic interferences on the Si isotope signals the
229 machine was run in "medium" resolution mode with a resolving power M/ΔM ~3300. Silicon
230 concentrations introduced into the machine were 2 ppm with average signal intensities on the
231 ^{28}Si ~ 10V. Isotopic compositions are reported in standard per mil notation ($\delta^{30}Si$) based on
232 blank-corrected isotope ratios calculated by a standard bracketing method using the NBS-28
233 (RM8546) silica sand internal standard (**eq. 1**):

234 $$\delta^{30}Si = \left[\frac{\left({}^{30}Si/{}_{28}Si \right)_{sample}}{AVG\left[\left({}^{30}Si/{}_{28}Si \right)_{std\text{-}I}, \left({}^{30}Si/{}_{28}Si \right)_{std\text{-}II} \right]} - 1 \right] \times 1000 \qquad (1)$$

235 where Std-I and Std-II refer to the NBS-28 standard measured directly before and after the
236 sample. Repeated evaluation (n= 21) of the international terrestrial basalt standard BHVO-2
237 yielded an average value -0.35‰ with a long-term precision for $\delta^{30}Si$ of ± 0.11‰ (2σ),
238 consistent with results of Savage et al. (2013), -0.28 ± 0.09‰ (2σ), for $\delta^{30}Si$ isotopic
239 measurements conducted in the same facilities at IPGP. Mass dependent fractionation for our
240 samples were verified through a three isotope plot where $\delta^{29}Si = \delta^{30}Si \times 0.5019$, $R^2 = 0.97$
241 (**Appendix A**).

242 **2.3 Transient model design**

243 Our transient model has the novel capability to calculate the depth into the mineral that
244 the fluid is able to interact and exchange with as a function of the mineral surface area. The
245 model is set up so that we can explicitly simulate stable isotope ratios of aqueous and
246 amorphous silica phases using a set of coupled TST (Transition State Theory; Aagaard and
247 Helgeson, 1982; Helgeson et al., 1984) rate laws for the rare and abundant ^{30}Si and ^{28}Si
248 isotopes (Druhan et al., 2013; **eq. 2a** and **eq. 2b**). The coupled equations are solved
249 numerically for a time-evolving approach to equilibrium, such that both the fluid and solid
250 isotopic composition are tracked during reaction progress.

$$^{28}R_p = {}^{28}X\,{}^{28}kA\left(\frac{{}^{28}SiO_{2(aq)}}{{}^{28}X\,{}^{28}K_{eq}} - 1\right)^m \quad (2a)$$

$$^{30}R_p = {}^{30}X\,{}^{30}kA\left(\frac{{}^{30}SiO_{2(aq)}}{{}^{30}X\,{}^{28}K_{eq}} - 1\right)^m \quad (2b)$$

$$R_p = kA\left(\frac{Q}{K_{eq}} - 1\right)^m \quad (2c)$$

Here the activity of each stable silicon isotope in the fluid phase is denoted as $SiO_{2(aq)}$, *A* refers to the reactive surface area (m^2), *k* is the forward rate constant (moles m^{-2} s^{-1}), K_{eq} is the equilibrium constant appropriate to the temperature of the experiments, and the reaction quotient, Q, quantifies the departure from equilibrium. A high order affinity dependence can be designated using the exponent *m*. Previous experimental studies of amorphous silica formation conducted in similar conditions (Iler, 1979; Fleming, 1986; Tobler et al., 2009) used an affinity term of 3.5 and we adopt this value for consistency. All stable isotopes of silicon other than ^{30}Si are implicitly treated in **eq. 2a**, representing approximately 97% of the total concentration, such that the sum of the net rates ($^{30}R_p$ and $^{28}R_p$) reasonably reproduces the total bulk silica precipitation rate (R_p, **eq. 2c**) even with the higher order dependence. The ^{i}X terms are defined as the mole fractions of the two stable isotopes of silicon in the appropriate phase (discussed below) and thus couple their individual rates, ^{30}Rp and ^{28}Rp (Druhan et al., 2013; Steefel et al., 2014; Druhan et al., 2015).

The extent of isotopic re-equilibration in this transient approach is dependent on the definition of the mole fraction ^{i}X (where *i* represents the isotope of interest, in this case either ^{28}Si or ^{30}Si) and the sum of ^{28}X and ^{30}X is equal to 1.0. How the mole fraction is defined dictates the extent to which the solid and fluid phases are allowed to re-equilibrate with one another (Druhan et al., 2013). In the case where the fluid does not interact with the solid phase (i.e. no back reaction), the mole fraction is represented by the aqueous composition. In the case where the fluid and solid phases could re-equilibrate with one another (partially or

completely), the mole fraction is represented by the solid phase, which may be defined in one of two ways. The simplest approach is to represent the solid isotope composition using the mineral volumes of the rare and common isotopologue such that ^{i}X is set to the isotope ratio of the "bulk" or total amorphous silica present (**eq. 3**).

$$^{i}X_{bulk}(t) = \frac{^{i}N_{SiO_2,\ init\ bulk}(t=0) + {}^{i}N_{SiO_2,cum.ppt}(t)}{\sum_i {}^{i}N_{SiO_2,\ total}(t)} \quad (3)$$

Here the mole fraction of each isotope of the bulk solid ($^{i}X_{bulk}$) at a given simulation time (t) is monitored through the addition of new mineral mass ($^{i}N_{SiO2\ cum.ppt}$) from the start of the simulation (t = 0) to the present time. This value is added to the initial mass of solid present in the system ($^{i}N_{SiO2,init\ bulk}$) throughout the duration of the precipitation reaction and divided by the total mass of solid for all isotopes present at that time $\left(\sum_i {}^{i}N_{SiO_2,\ total} = {}^{i}N_{SiO_2,\ init\ bulk}(t=0) + {}^{i}N_{SiO_2,cum.ppt}(t)\right)$, assuming an ideal solid solution. This approach is thus distinct from more traditional homogeneous type models where re-equilibration with the bulk is assumed to be instantaneous (Curti et al., 2005; Curti et al., 2010; Handler et al., 2014; Joshi et al., 2017; Gorski and Fantle, 2017). Under this "bulk" approximation, the system effectively allows the isotopes of the fluid and the entire solid phase to re-equilibrate through time, as though the solid phase has an infinite surface area (i.e. unable to isotopically zone), such that the fluid interacts with the isotopic composition of the bulk solid. The second approach is to approximate the unique isotope ratio of the most recently formed mineral surface (i.e. distinct from the interior or bulk) and allow this to communicate with the surrounding fluid. In continuum scale models (such as the one used in this study), this value cannot be explicitly tracked through a discretized volume-averaged solid phase. Therefore, we approximate the mineral surface isotopic composition using a running average of the isotope ratio of the silicon that just precipitated out of solution over a given time interval (t - T) that the user can choose (**eq. 4**).

$$^{i}X_{surface}(t) = \frac{^{i}M_{SiO_{2,aq}}(t\text{-}T) - ^{i}M_{SiO_{2,aq}}(t)}{\sum_{i}\left(^{i}M_{SiO_{2,aq}}(t\text{-}T) - ^{i}M_{SiO_{2,aq}}(t)\right)} \qquad (4)$$

Where t is again the current time reached in the simulation, T is the lower bound of this time interval ($T < t$) to perform the running average of the concentration of $^{30}SiO_{2,aq}$ and $^{28}SiO_{2,aq}$ most recently removed from solution ($^{i}M_{SiO_{2,aq}}$), and the mole fraction ($^{i}X_{surface}$) is calculated as $^{i}M_{SiO_{2,aq}}$ divided by the total for both isotopes ($\sum_{i} {}^{i}M_{SiO_{2,aq}}(t-T) - {}^{i}M_{SiO_{2,aq}}(t)$). The lower bound of the time interval is defined by two distinct parameters: (1) the numerical model timestep, Δt, which is a fixed parameter dictated by the numerical model stability criteria, and (2) the number of timesteps to average over, A, which is a user specified parameter that we can adjust to constrain the time interval appropriate for each experimental data set ($T = \Delta t \times A$).

It is important to note that the variable A is not an arbitrarily created free parameter, but has physical meaning within our experimental design. Each experimental dataset reported in the present study features a unique surface area, meaning that the same mass of newly formed mineral is distributed over distinct total solid phase areas and thus the depth of this newest layer differs. The fluid-interaction depth then dictates the amplitude of kinetic fractionation and the apparent rate of isotopic re-equilibration observed between the fluid and bulk solid (discussed further in **Section 4.4**). By adjusting A between experiments, we are thus able to impose unique time intervals to average over, which then provide a proxy for the fluid-mineral interaction depth over a known surface area. This correlation between the amount of solid phase precipitated on a given surface area over a given time interval and the depth into the surface that the fluid can isotopically exchange with is a key feature of the modeling framework. Use of this running average time interval in our transient model thus provides a novel approach to estimating the fluid-mineral surface interaction depth during crystal growth.

Finally, we note that the use of a higher order affinity term as implemented here (**eq. 2**) for amorphous silica formation does not strictly allow the fluid and solid (or solid surface) defined by the mole fraction to attain the imposed equilibrium fractionation factor at the limit where isotopic re-equilibration should be complete (as it would using a linear rate expression). For the vast majority of experimental data reported herein, this behavior exerts negligible influence on the corresponding model results. Where isotopic re-equilibration is suggested to have occurred extensively, the effect of this limitation is discussed in detail.

3. RESULTS

3.1 Aqueous chemistry

Results from the three amorphous silica precipitation experiments conducted at similar pH (~7), saturation states (initial log Q/K_{sp} = 0.48 oversaturated with respect to amorphous silica), for a range of different mineral surface areas (50 $m^2\ g^{-1}$ to 0.072 $m^2\ g^{-1}$) are presented in **Table 2.** Aqueous silica and corresponding $\delta^{30}Si$ isotope ratios for the duration of the three experiments are shown in **Fig. 1**. Dissolved silica concentrations with time show distinct trends between the high, medium, and low surface area cases (**Fig. 1A**). The high SA experiment exhibits an initial, rapid decrease in dissolved silica concentrations during the first 2 days, followed by a gradual approach to equilibrium over a period of ~30 days. Notably, after 30 days, the high SA experiment reached dissolved silica levels ~13% above the theoretical amorphous silica solubility concentration of 1.75 mM at 20°C (Gunnarsson and Anórsson, 2000). In the medium and low SA experiments, silica concentrations decrease during the first 5 days and appear to stabilize at $SiO_{2(aq)}$ values of ~3 mM and ~4 mM, approximately 1.7× and 2.3× the solubility concentrations, respectively. Aqueous silica concentrations in all cases were well above the theoretical solubility concentration and at saturation states greater than 0 at the end of the experimental runs (~30 days).

3.2 Precipitation rates

Time-averaged precipitation rates normalized to the surface area, R_p (reported as mol m^{-2} s^{1}) were calculated for all three batch runs by the following expression (**eq. 5**):

$$R_p = \frac{N_{SiO_{2(ppt)}\ t_I} - N_{SiO_{2(ppt)}\ t_{II}}}{S \cdot \Delta t_{II-I}} \qquad (5)$$

where the instantaneous amount of amorphous silica precipitated out of solution ($N_{SiO2(ppt)}$), defined in units of moles, is obtained through the decrease in aqueous silica concentrations multiplied by the volume of fluid in the reactor at the time of sampling over a given time interval ($\Delta t_{II-I} = t_{II} - t_I$) in units of seconds and normalized to the reactive surface area, S (m^2). The reactive surface area (S) is calculated based a volume-correction that accounts for solid phase lost via sampling at each given time (further details are addressed below in **Section 4.1**). Initial precipitation rates for the high, medium, and low SA experiments were $10^{-9.48}$ mol m^{-2} s^{-1}, $10^{-8.62}$ mol m^{-2} s^{-1}, and $10^{-8.47}$ mol m^{-2} s^{-1} and systematically decreased throughout the course of the experiment.

3.3 Silicon isotopes

Like the concentration trends, fluid $\delta^{30}Si$ express high sensitivity to the range of surface areas tested (**Fig. 2B**). For all three experiments, initial fluid $\delta^{30}Si$ are −2.08 ± 0.11‰ (2σ). In comparison the initial average bulk amorphous $\delta^{30}Si$ value was measured before (−1.77 ± 0.05‰ (2σ), n=3) and at the end of the experiments, and final values were not significantly different than initial values (−1.81 ± 0.03‰ (2σ) n=3, −0.04‰ difference). Early stages of precipitation were generally characterized by an increase in fluid phase $\delta^{30}Si$. The highest SA case reached a maximum fluid $\delta^{30}Si$ of −1.03 ± 0.04‰ (2σ) (1.00 ± 0.06‰ (1σ)) enrichment with respect to starting value) within ~22 hours that was then followed by a reversal back towards lower values (−2.22 ± 0.05‰ (2σ), n=3). For this high SA case, the $\delta^{30}Si$ of the fluid stabilized at values significantly more negative than the bulk solid by −0.32 ± 0.06‰ (2σ). For the medium SA experiment, fluid $\delta^{30}Si$ reached a maximum value of -0.71 ± 0.14‰ (2σ) (1.34 ± 0.11‰ (1σ) greater than the starting fluid value). Relative to the high SA condition,

this enrichment takes place over a longer period of time (~12 days) and remains at relatively elevated values for the duration of the experiment. The low SA experiment attained a maximum fluid $\delta^{30}Si$ of -1.14 ± 0.04‰ (2σ) at ~24 days, corresponding to an enrichment of 0.90 ± 0.10‰ (2σ) above the initial fluid $\delta^{30}Si$ that, like the medium SA case, stabilizes for the remainder of the experiment. For both the medium and low SA experiments, the subsequent reversal towards initial fluid $\delta^{30}Si$ values observed in the high SA case is not captured, as shown by $\delta^{30}Si$ stabilizing at elevated values after ~1 week. Critically, in all three experiments, fluid $\delta^{30}Si$ values are distinct from the bulk amorphous silica composition at the end of the experimental duration.

Assuming a closed system, the $\delta^{30}Si$ value of newly precipitated amorphous silica accumulated through time over the duration of the experiment ($\delta^{30}Si_{ppt}$) was calculated using isotopic mass balance formulations based on the initial moles of dissolved silica ($N_{SiO_{2aq,i}}$), the corresponding initial silicon isotope composition ($\delta^{30}Si_{aq,i}$), the dissolved silica in solution at a given point in time ($N_{SiO_{2,aq}}$) and its corresponding $\delta^{30}Si_{aq}$ (**eq. 6**).

$$\delta^{30}Si_{ppt} = \frac{N_{SiO_{2aq,i}} \cdot \delta^{30}Si_{aq,i} - N_{SiO_{2,aq}} \cdot \delta^{30}Si_{aq}}{N_{SiO_{2,ppt}}} \quad (6)$$

The mass of silica precipitated ($N_{SiO2,ppt}$) was determined by subtracting the dissolved silica at a given sampling time from the initial amount (**Table 2**). Error presented in **Table 2** was calculated to 1σ using standard error propagation using three formulas: $\sigma_{a,b} = \sqrt{\left(\frac{\sigma_{N_{SiO_{2,aq}}}}{N_{SiO_{2,aq}}}\right)^2 + \left(\frac{2\sigma_{\delta^{30}Si_{aq}}}{\delta^{30}Si_{aq}}\right)^2} \times (N_{SiO_{2,aq}} \cdot \delta^{30}Si_{aq})$, sum of squares: $\sigma_c = \sqrt{(\sigma_a)^2 + (\sigma_b)^2}$, and $\sigma_{\delta^{30}Si_{ppt}} = \sqrt{\left(\frac{\sigma_c}{N_{SiO_{2aq,i}} \cdot \delta^{30}Si_{aq,i} - N_{SiO_{2,aq}} \cdot \delta^{30}Si_{aq}}\right)^2 + \left(\frac{\sigma_{N_{SiO_{2,ppt}}}}{N_{SiO_{2,ppt}}}\right)^2} \times \delta^{30}Si_{ppt}$.

392 Observed fractionation factors (α_{obs}) are calculated as the difference between $\delta^{30}Si$ values
393 of dissolved silica ($\delta^{30}Si_{aq}$) and the corresponding precipitated amorphous silica ($\delta^{30}Si_{ppt}$) at
394 each sampling time (**eq. 7**).

395 $$\alpha_{obs} = \frac{\left(\delta^{30}Si_{ppt} + 1000\right)}{\left(\delta^{30}Si_{aq} + 1000\right)} \qquad (7)$$

396 $\delta^{30}Si_{ppt}$ values were calculated according to the same isotopic mass balance formulations used
397 in **eq. 6** (**Table 2**). Notably this definition follows the calculations used in Roerdink et al.
398 (2015) and thus allows direct comparison. Observed fractionation factors and precipitation
399 rates appear to be inversely correlated, where α_{obs} is generally seen to increase as R_p (eq. 5)
400 decreases in the approach to near equilibrium conditions. The high SA experiment expresses
401 the largest range in α_{obs} values from 0.9963 ($\Delta^{30}Si_{ppt\text{-}fluid} = -3.73 \pm 0.20‰$) at an initial R_p of
402 $10^{-9.48}$ mol m^{-2} s^{-1} to 1.0002 ($\Delta^{30}Si_{ppt\text{-}fluid} = +0.24 \pm 0.15‰$) at an R_p of $10^{-12.49}$ mol m^{-2} s^{-1} near
403 the end of the experiment when concentrations and isotope ratios reach steady state values.
404 The medium and low SA experiments produced α_{obs} values of 0.9959 ($\Delta^{30}Si_{ppt\text{-}fluid} = -4.12 \pm$
405 0.20‰) and 0.9956 ($\Delta^{30}Si_{ppt\text{-}fluid} = -4.42 \pm 0.22‰$) respectively. Comparison between the
406 three experiments, together representing a broad surface area range from 50 – 0.072 m^2/g ,
407 show clear differences in both the magnitude and evolution in the observed fractionation
408 factor as a function of reaction progress.

409 ## 4. DISCUSSION

410 ### 4.1 Tracking surface area during precipitation

411 Changes in the surface area of seed crystals during precipitation can potentially become
412 significant enough to influence the reaction rate. Assuming homogeneous growth onto pre-
413 existing spherical grains, the mass removed from solution in our experiments relative to the
414 mass of the starting seed crystals would correspond to an increase in total surface area on the
415 order of <0.01% (Steefel and Lasaga, 1994; Steefel and Lichtner, 1998; Gunter et al., 2000).

These assumptions are reasonable, given that precipitation onto existing mineral surfaces in this temperature range is far more energetically favorable than overcoming a nucleation barrier (Iler, 1979). However, as in the similar experimental design used by Roerdink et al. (2015), the process of sampling inherently removes some of the suspended solid phase. As a result, the total surface area of the solid available for precipitation in fact decreases over the duration of the experiment. This somewhat counterintuitive behavior exerts a much stronger influence on the overall surface area, as for example the 37% decrease reported by Roerdink et al. (2015). In the present study we constrain this loss of total surface area due to sampling by reporting a volume-corrected surface area (S) calculated by multiplying the initial total surface area of amorphous silica present in the reactor (in units of $m^2\ L^{-1}$) by the reactor volume at a given time, t. The initial total surface areas per unit volume for the high, medium, and low SA experiments were 495 $m^2\ L^{-1}$, 2.17 $m^2\ L^{-1}$, and 1.25 $m^2\ L^{-1}$ respectively. In our experiments the loss in total surface area was lower than that reported by Roerdink et al. (2015) due to the smaller volume of each sample, resulting in overall decreases of 19.8%, 9.6% and 7.9% for the high, medium and low surface areas, respectively (m^2, **Table 2**).

4.2 Influence of surface area on amorphous silica solubility

Observations of dissolved silica concentrations stabilizing to distinct values at the end of the three experiments (**Fig. 1A**) suggest that surface area could exert a direct control on amorphous silica solubility (Parks,1984; Williams et al.,1985). Standard calculation of thermodynamic equilibrium constants does not include a surface area dependence. Thus, to account for this possibility, a correction was performed on the amorphous silica equilibrium concentration determined at 20℃ (Gunnarsson and Anórsson, 2000) using the Freundlich-Ostwald equation (Enüstün and Turkevich, 1960). No significant differences in solubility concentrations were found between the three amorphous silica precipitation cases (**Appendix**

440 **B**). Therefore, we conclude that direct surface area control on amorphous silica solubility is
441 unlikely over the range of surface areas used in this study.

442 Having verified that the equilibrium state is the same for all experiments, we may now
443 determine the extent to which thermodynamic equilibrium was established for each surface
444 area case. Despite reactions having slowed to rates indistinguishable from zero and dissolved
445 silica concentrations having stabilized at constant values, calculated saturation states (**Table**
446 **2**) indicate that only a metastable equilibrium was reached. Thus, from this point forward, we
447 refer to a period of "metastable equilibrium" corresponding to the time interval over which a
448 steady state concentration is observed and discernable net precipitation has ceased. Notably,
449 this observation is consistent with two prior amorphous silica precipitation studies, one
450 involving a closed batch reactor (Roerdink et al., 2015) and the other using flow-through
451 experiments (Geilert et al., 2014), both of which both demonstrated what they termed
452 equilibrium fractionation endmember behavior under these meta-stable conditions.

453 This emerging observation of "metastable equilibrium" in both previous publications and
454 the present study points to a complexity in the establishment of true thermodynamic
455 equilibrium for amorphous silica phases. If thermodynamic equilibrium is difficult to achieve
456 in these highly controlled laboratory environments, then similar complexities may influence
457 open and transient flow environments. If we consider that these natural environments
458 commonly host longer fluid residence times and sustain slower water-rock interactions than
459 can be reasonably constrained in the lab, then we may anticipate that these systems are better
460 able to establish true thermodynamic equilibrium with such silica phases. However, natural
461 environments are also commonly subject to variable boundary conditions and other forms of
462 periodic or transient behavior, which may promote similar metastable equilibria. In this case,
463 the application of traditional methods using simple K_{eq} calculations to characterize the
464 thermodynamics of secondary amorphous silica reactions occurring in low temperature

weathering systems would be insufficient. Though beyond the scope of the current study, which focuses on the recording and exchange of isotopic signatures across the fluid – mineral boundary, we suggest these observations warrant further investigation.

4.3 The distinct effects of surface area on precipitation rates

As expected, surface area exerts a principle control on precipitation rates. This effect can be clearly discerned in the present experiments through comparison between overall bulk precipitation rates (R_{bulk}, **Table 2**) and precipitation rates normalized to the total available surface area (R_p, **Table 2**). Assuming homogeneous precipitation, higher surface area seeds yielded overall faster precipitation rates as a direct consequence of more mineral surface available (25 m^2) for the reaction to occur. The total amount of surface available for the medium and low SA cases was 2 orders of magnitude less than the high SA batch (0.54 m^2 and 0.31 m^2 respectively) and bulk precipitation rates were proportionally lower given comparable starting values of oversaturation. However, when these rates are normalized to the surface area (following the same reporting as both Geilert et al., 2014 and Roerdink et al., 2015) we obtain much closer values between the three conditions that all agree with previously reported amorphous silica precipitation rates: $R_p = 10^{-9.67}$ mol m^{-2} s^{-1} (Rimstidt and Barnes, 1980), $10^{-9.57}$ mol m^{-2} s^{-1} (Geilert et al., 2014), and $10^{-9.00}$ mol m^{-2} s^{-1} (Roerdink et al., 2015).

The amount and thickness of amorphous silica precipitated out of an initially oversaturated solution and onto the surfaces of pre-existing seeds is somewhat more complex, in that there is a dependence on both the total masses of silicon present as a solid and in solution (solid:fluid mass ratio) and the surface area of the seed crystals (assuming that amorphous silica is precipitated homogeneously onto the entire surface of each individual grain). These two distinct physical characteristics of the system, the solid:fluid mass ratio and the surface area, regulate the thickness of the newly-formed mineral surface that can be

490 formed. As a result, individual constraint of either the solid:fluid mass ratio or the surface
491 area of the seed crystals would be insufficient to estimate the thickness of new precipitate
492 accumulated during mineral formation. The present study demonstrates the relative effects of
493 these two parameters. The medium and low SA experiment solid:fluid mass ratios (50
494 $SiO_{2(s)}$:$SiO_{2(aq)}$ (g/g)) are greater than the high SA value (~31 $SiO_{2(s)}$:$SiO_{2(aq)}$ (g/g)). This
495 difference resulted from the use of both a larger fluid volume and more seed crystals in the
496 medium and low SA design (**Table 1**) and would inherently suggest that the high SA
497 experiment should form a thicker layer of new precipitate. However, following this simple
498 calculation the corresponding accumulated depth values were 35 nm and 45 nm for the
499 medium and low SA experiments, respectively, in comparison to only 0.22 nm for the high
500 SA experiment (in agreement with numerical simulation results discussed in **Section 4.5.1**).
501 Thus, even though the medium and low SA systems had higher solid:fluid mass ratios, their
502 lower surface areas contributed to a much thicker depth of newly accumulated material onto
503 the mineral surfaces.

504 **4.4 Models for silicon stable isotope fractionation**

505 Stable isotope fractionation for reversible secondary mineral formation reactions such as
506 amorphous silica precipitation can be characterized by the balance of the forward
507 precipitation rate, R_f, and the backward dissolution rate, R_b, between a mineral and its
508 surrounding fluid (**Fig. 2**). The net rate (R_p) reflects a condition in which $R_f > R_b$ such that the
509 mineral is actively forming and fluid solute concentrations are decreasing with time (**Fig. 2A**).
510 In this scenario, most stable isotope systems undergo kinetic fractionation where the "light"
511 isotope is preferentially incorporated into the solid phase, leaving the remaining solution
512 enriched in the "heavy" isotope (DePaolo, 2004). For a system starting at equivalent fluid and
513 solid stable isotope ratios, kinetic fractionation associated with precipitation ($\alpha_{kin} \neq 1.0$) of a
514 secondary precipitate results in a characteristically large shift in the fluid isotope ratio towards

515 stable isotope values distinct from the bulk composition (i.e. “kinetic enrichment”). A unique
516 feature of reversible secondary mineral precipitation is the establishment of a dynamic
517 equilibrium (**Fig. 2B**), where the net rate slows down as the backward and forward rates
518 become equal to one another ($R_f = R_b$) and ultimately ceases ($R_p = 0$). In this state of dynamic
519 chemical equilibrium, continued isotope exchange between the fluid and solid phase as a
520 result of equilibrium fractionation ultimately returns the system towards equilibrium delta
521 values (i.e. “isotopic re-equilibration”). A major consequence of this unique isotopic re-
522 equilibration timescale is that the observed fractionation will vary with reaction progress (R_p)
523 as the initially kinetic isotopic signature generated from precipitation transitions to values
524 reflecting the establishment of chemical equilibrium. For a system in which $\alpha_{eq} = 1.0$, this
525 process would return the fluid isotope ratio to a value equivalent to the solid phase (Druhan et
526 al., 2013; Steefel et al., 2014).

527 Therefore, the isotope ratio chosen to represent the solid phase is a critically important
528 parameter for determining the extent of isotopic re-equilibration in the fluid-mineral system.
529 Traditionally, many “batch” or “steady state” models commonly employed in predicting
530 isotope fractionation from catchment to mineral scales (Bouchez et al., 2013) choose to
531 represent the solid phase as the composition of the entire “bulk” mineral. Underlying this
532 assumption is the notion that the solid phase has a homogenous composition that remains at
533 “steady state” ($d(^{i}N/^{j}N)/dt = 0$, where N = element and *i,j* = given stable isotope) throughout
534 mineral growth and interacts entirely with the surrounding fluid. Under such conditions, the
535 isotope ratio of the fluid phase is heavily influenced by the mass of the bulk solid and rapidly
536 shifts back to the bulk isotope value for $\alpha_{eq} = 1.0$ following kinetic perturbation (**Fig. 2C**).
537 While this approach is reasonable for some systems, such as the extremely high surface areas
538 associated with carbonate foraminifera (Keir, 1980; Halbach and Puteanus, 1984; Walter and
539 Morse, 1985; Morse et al., 2007, and others), for the majority of terrestrial weathering

environments characterized by highly variable fluid chemistry and a wide range of mineral surface areas and grain sizes (Peters, 2009; Landrot et al., 2012), it's unlikely that the solid isotope composition could be reasonably represented by the bulk mineral value (Johnson et al., 2002; Wiederhold et al., 2006; Kiczka et al., 2010).

For natural, open systems a more reasonable representation of the solid isotope composition would be the isotope ratio of the mineral surface co-evolving with the surrounding fluid ($d(^{i}N/^{j}N)/dt \neq 0$, **Fig. 2D**). Following a kinetic perturbation, precipitation would first kinetically fractionate the fluid, enriching it in the "heavy" isotope, while, through mass balance, the resulting precipitate would form a new mineral surface layer this is isotopically "light" in comparison. As this growth phase slows down and approaches equilibrium, the mineral becomes isotopically zoned and increasingly enriched in the light isotope. Evidence for the formation of such isotopically zoned minerals during crystal growth has been extensively reported (e.g. Skulan et al., 2002; Wiederhold et al., 2006; Kiczka et al., 2010). Ultimately, the net precipitation rate becomes negligible and at these near-equilibrium conditions, isotopic re-equilibration beings to occur. In the approach to dynamic equilibrium, the mineral surface mirrors the fluid isotopic behavior, losing its kinetic signature as isotopic exchange shifts the system towards delta values reflective of equilibrium fractionation between the fluid and the amount of newly formed mineral surface that is actively exchanging. In this approach, the extent and timing of fluid and solid phases isotopically re-equilibrating with one another should be dependent on the depth into the mineral surface that the fluid can access, which is dictated by the mineral surface area.

Therefore, the mineral surface area is predicted to exert a first order control on the extent of fluid-mineral chemical and isotopic exchange during secondary mineral formation. To test this hypothesis, we apply three different isotope fractionation models to our experimental results: (1) A Rayleigh distillation model where the fluid is assumed to be isolated from any

565 exchange with the solid phase, (2) A steady state surface reaction kinetic model where the
566 fluid only interacts with a constant solid surface composition, and (3) A modified-transient
567 model developed in this study (section 2.3) that allows for the fluid and solid to interact and
568 isotopically co-evolve.

569 ***4.4.1 The Rayleigh model: A kinetic perspective***

570 Rayleigh distillation models have been successfully used to interpret silicon isotope
571 fractionation in multiple prior studies (De La Rocha et al., 1998; R B Georg et al., 2007;
572 Opfergelt and Delmelle, 2012; Reynolds, 2012; Pogge von Strandmann et al., 2012; Hughes
573 et al., 2013). Under the assumption of a well-mixed, closed, and kinetically controlled system,
574 in which a mineral is irreversibly precipitated from solution as a reaction product subject to a
575 single fixed fractionation factor, the isotopic distillation of the residual reactant can be
576 described as $R = R_0 \cdot f^{(\alpha_{kin} - 1)}$ (Rayleigh, 1902). In this expression, the instantaneous isotope
577 ratio of the reactant pool (R) is equal to its initial isotope ratio (R_0) multiplied by the fraction
578 of reactant remaining in solution with respect to its starting concentration (f), which is raised
579 to the power ($\alpha_{kin} - 1$) where the fractionation factor (α_{kin}) is constant.

580 Given the success with which Rayleigh approaches have been used in prior Si studies, we
581 begin our analysis of the present amorphous silica precipitation experiments using this
582 framework. However, it is immediately apparent that a Rayleigh model using a fixed
583 fractionation factor of 0.9967 (Roerdink et al., 2015) fails to capture the variability in both
584 measured fluid $\delta^{30}Si$ and $\delta^{30}Si$ of the cumulative precipitated amorphous silica calculated
585 according to closed system, mass balance (**Section 3.3, eq. 6**) as a function of reaction
586 progress (**Fig. 3**). In all three batch datasets, the Rayleigh model reasonably reproduces the
587 trend in fluid isotope enrichment early in the experiment (when precipitation rates are high),
588 but systematically over-estimates the evolution of fluid $\delta^{30}Si$ as precipitation rates slow down
589 in the approach to metastable equilibrium. As a consequence, experimental $\delta^{30}Si$ values

590 appear to “fall off” the Rayleigh line. This general observation is also supported by data
591 generated in similar amorphous silica batch experiments using identical high surface area
592 grains (50 m^2/g) reported by Roerdink et al. (2015) (**Fig. 3A**). Notably, the extent to which
593 the experimental data deviate from Rayleigh fractionation appears to differ between the
594 unique values of surface area. Additionally, calculated $\delta^{30}Si$ of the cumulative precipitated
595 amorphous silica are more elevated than the Rayleigh predictions and appear to follow a
596 general trend that roughly coincides with the prediction of the instantaneous precipitate.
597 There are several possible explanations for the observed misfit between our
598 experimental data and the Rayleigh model. The quality of reagents used to prepare the
599 solutions and starting amorphous silica grains minimize the potential for any significant
600 sorption processes involving impurities like iron oxides (Delstanche et al., 2009) or aluminum
601 hydroxides (Oelze et al., 2014) that could influence fluid $\delta^{30}Si$. Additionally, the effects of
602 partially open system behavior or incomplete separation of one phase relative to the other are
603 negated by the experimental and sampling design. Another possibility is that additional
604 fractionation factors may be influencing the system due to precipitation of multiple silica
605 polymorphs such as cristobalite and quartz during the course of the reaction. However, this
606 effect is unlikely given that the saturation states attained in these experiments coupled with
607 the purity of the initial amorphous silica seeds makes the formation of these alternative
608 polymorphs energetically unfavorable.
609 Thus, a more likely cause for variability in the fractionation factor is due to non-negligible
610 back-reaction from the solid phase to the fluid as a result of the approach to equilibrium. Such
611 mixed contributions from both kinetic and equilibrium isotope effects lead to an overall
612 fractionation factor that is not constant through time and thus violates the assumptions
613 inherent in Rayleigh distillation. Evidence for this behavior is best shown in the high SA
614 experiment (**Fig. 3B**) where fluid $\delta^{30}Si$ deviate quickly from Rayleigh predictions due to fast

615 reaction kinetics pushing the system rapidly towards equilibrium and ultimately converging to
616 values equivalent to the precipitated amorphous silica $\delta^{30}Si$ at the end of the experiment. In
617 order to reach these nearly equivalent values of fluid and precipitated amorphous silica phases
618 at near-equilibrium conditions, isotopic exchange must have occurred. Departure of the
619 medium (**Fig. 3C**) and low (**Fig. 3D**) surface area fluid $\delta^{30}Si$ from the Rayleigh trend is
620 comparatively smaller than what was observed for the high surface area data, as these systems
621 featured slower kinetics. But, the fluid values of both eventually start to converge back
622 towards the amorphous silica precipitate $\delta^{30}Si$ near the end of the experiments. In all
623 examples, the effect of the approach to equilibrium is to diminish the magnitude of the kinetic
624 fractionation factor, leading to overall or effective values closer to 1.0. As a result, the
625 cumulative precipitate becomes increasingly less fractionated relative to the fluid, which gives
626 the appearance of matching the instantaneous product Rayleigh prediction rather than the
627 cumulative value if the fractionation factor had remained constant.

628 Ultimately, the Rayleigh fractionation model assumes that the product pool is
629 instantaneously isolated such that no reversal or back-reaction can occur. The present data do
630 not satisfy this requirement, as contributions from the back reaction are apparent. Application
631 of a constant, kinetic fractionation factor to represent the overall effective fractionation factor
632 of this reversible amorphous silica precipitation reaction leads to predictions of $\delta^{30}Si$
633 fractionation that, in this case, highly over-estimate our observations. Thus, we proceed by
634 considering a model framework that allows for variability in the observed fractionation factor
635 as a result of combined kinetic and equilibrium effects.

636 ***4.4.2 A steady state model for mixed kinetic and equilibrium behavior***

637 A stable isotope framework that can predict the observed fractionation factor (α_{obs}) at
638 steady state resulting from a balance between kinetic and equilibrium effects is provided by
639 the surface reaction kinetic model (DePaolo, 2011). This approach has been successfully

applied to quantify the fractionation observed for two prior amorphous silica precipitation studies (Geilert et al. 2014; Roerdink et al. 2015) and has since begun to be discussed in the interpretation of $\delta^{30}Si$ signatures in weathering environments (Frings et al. 2016). This steady state model takes the form of an analytical solution where α_{obs} is predicted based on mixed contributions from both kinetic (α_{kin}) and equilibrium (α_{eq}) isotopic fractionation end members, which vary as a function of the balance between forward precipitation (R_p) and backward dissolution (R_b) rates (eq. 10 in DePaolo, 2011) .

Application of the steady state model to our experimental results show that α varies systematically with experimentally constrained values of R_p (**Section 3.2; Table 2**), lying principally within the transitional zone between the kinetic (lower plateau) and equilibrium (upper plateau) endmembers (**Fig. 4**). Steady state model predictions for an α_{kin}= 0.9967 and α_{eq} = 1.0002 agree with the earlier Roerdink et al. (2015) results (**Fig. 4A)** and our high surface area α_{obs} values (**Fig. 4B)**. The large variability observed in these high surface area cases as a function of reaction progress suggests significant effects of the equilibrium end member and thus isotopic re-equilibration. Arguments for dismissing other potential processes that can cause variability in the fractionation factor such as neo-formation of polymorphs or the precipitation of additional secondary phases have been discussed in detail in **Section 4.4.2**. Medium (**Fig. 4C)** and low (**Fig. 4D**) surface area α_{obs} values plot preferentially closer to the kinetic endmember as a function of precipitation rate and reflect relatively less isotopic re-equilibration.

The equilibrium fractionation factor between $SiO_{2(aq)} \leftrightarrow SiO_{2(am)}$ has yet to be constrained experimentally, and thus α_{eq} = 1.0002 was estimated by taking the reciprocal of eqn. 10 (DePaolo, 2011), and applying a linear regression analysis on $\frac{1}{\alpha_p}$ vs. $\frac{R_p}{R_p+R_b}$ for the high SA experiment where near-equilibrium conditions were obtained. The unidirectional dissolution rate, R_b (1.95×10^{-11} mol m^{-2} s^{-1} at pH = 7.5) is set to a fixed value based on

665 dissolution experiments using the same high surface area amorphous silica crystals
666 (Loucaides et al., 2008). Although R_b is treated as a constant in the present study, DePaolo
667 (2011) suggested a second approach in which R_b scales as a function of R_p. We have elected
668 to use the version of the surface kinetic model which assumes a constant R_b for two principle
669 reasons. First, at present, there are no reliable constraints on the functional form of the
670 relationship between R_b and R_p for amorphous silica precipitation. Second, this approach is in
671 agreement with two prior studies utilizing the same fixed R_b model framework for Si
672 precipitation, thus allowing us to draw direct comparison to their results. As a final check we
673 attempted to fit our present dataset using the $R_b = R_p^{1/2}$ functional form proposed for calcite
674 (DePaolo, 2011), but failed to reproduce observed α variability with this approach. Thus,
675 further work is necessary before we can defensibly suggest any variability in R_b for
676 amorphous silica precipitation and associated implications for observed fractionation factors.
677 The initial observed fractionation for the high SA experiment (ε_{obs} = -3.73‰) is smaller
678 than those observed at the start of the medium (ε_{obs} = -4.12‰) and low (ε_{obs} = -4.42‰) SA
679 experiments. The corresponding α_{kin} (0.9967) value which reasonably captures both the
680 Roerdink et al. (2015) dataset and our high SA experiment (**Fig. 4, solid black line**) similarly
681 fails to capture the evolution of the initially high α_{obs} values for the low (0.9954) and medium
682 (0.9959) surface area conditions. These higher initial α_{obs} may imply either larger kinetic
683 fractionation in the medium and low SA experiments or the presence of transient effects
684 influencing the silicon isotope behavior. However, implementing unique α_{kin}values of 0.9959
685 (**Fig. 4C, dashed line**) and 0.9956 (**Fig. 4D, dotted line**) to account for differences in the α_{kin}
686 endmember of the medium and low SA cases is unable to capture the subsequent evolution of
687 α_{obs} as a function of R_p. Thus, differences in the largest observed fractionation factors
688 between the three surface area experiments imply an influence of transient isotope behavior
689 arising from the progressive growth of amorphous silica from an isotopically evolving fluid.

690 This behavior is inconsistent with the assumptions of DePaolo (2011) model, which is based
691 on a steady state mineral surface composition. Thus, we now seek to provide a novel
692 framework based on the influence of the physical characteristics of the system (i.e. surface
693 area and solid:fluid mass ratios) on kinetic behavior through a transient model capable of
694 characterizing the isotopic co-evolution of the fluid and growing mineral surface.

695 ***4.4.3 A transient model for mixed kinetic and equilibrium behavior***

696 To explore the effects of surface area and solid to fluid ratios in a fully transient
697 framework, we developed a numerical model (described in **Section 2.3**) using CrunchTope,
698 an isotope-enabled, multi-component reactive transport software (Steefel et al., 2015). The
699 input parameters used for our numerical simulations corresponded to the experimental
700 conditions for each of the three datasets with distinct surface area values (**Table 3**). Across all
701 simulations we used one common set of reaction rate constants, initial aqueous silica
702 concentrations, and kinetic and equilibrium fractionation factors for all three experiments.
703 The only parameters that vary between the three cases are the surface area and the solid to
704 fluid ratios. Before applying our transient model to the $\delta^{30}Si$ batch data, we first verified that
705 the simulation reproduced our experimental $SiO_{2(aq)}$ concentrations and found good agreement
706 (**Fig. 5A**) using a TST (Transition State Theory) rate expression (**eq. 2**) of order m = 3.5
707 (justification is provided in **Section 2.3**).

708 Experimentally determined $\delta^{30}Si$ data were then simulated using three separate isotopic
709 fractionation models: (1) a "no back-reaction" model (**Fig. 5B**), (2) a steady state ("bulk")
710 model (**Fig. 5C**), and (3) a transient ("mineral surface") model (**Fig. 5D**). In the "no back-
711 reaction" simulation, isotope fractionation is strictly kinetic, $\alpha_{obs} = \alpha_{kin}$ (0.9967), analogous to
712 models utilized previously for simplified fractionation during mineral precipitation (e.g. Curti
713 et al., 2005; Curti et al., 2010; Druhan et al. 2014; Joshi et al., 2017; Gorski and Fantle, 2017).
714 Limited by a strictly kinetic approach (i.e. no isotopic re-equilibration), the "no back-

reaction" model fails to reproduce measured fluid $\delta^{30}Si$ variability with time. In the "bulk" simulation, the fluid is allowed to isotopically re-equilibrate with the entirety of the bulk mineral composition , ${}^{i}X_{bulk}$ (**eqn. 3**), that is tracked through time in the model. In this approach, the bulk $\delta^{30}Si$ remains unchanged throughout the reaction because the addition of precipitate is small relative to the initial mass present in the system. Application of this "bulk" model under-estimates the kinetic fractionation observed in the fluid $\delta^{30}Si$ of all three experiments as a result of a large influence from the bulk $\delta^{30}Si$ value due to its comparatively large mass. Notably, the high SA case is predicted to have both a smaller extent of silicon isotopic re-equilibration and continued disequilibrium between the fluid and amorphous silica phases at the end of the experiment. A lack of agreement between the "bulk" model and the experimental $\delta^{30}Si$ data implies that fluid interaction with the entirety of the bulk amorphous silica is unlikely under this given range of surface areas.

In our final "mineral surface" simulation (**Fig. 5D**), the fluid is allowed to isotopically re-equilibrate with a co-evolving mineral surface during mineral growth, ${}^{i}X_{surface}$ (**eqn. 4**). As described earlier (**Section 2.3**), the amount of the mineral surface that the fluid is allowed to interact with is estimated in this model by a unique time interval over which a running average of the isotopic composition of the amorphous silica precipitating out of solution is calculated (t - T, where $T = \Delta t \times A$). The time intervals are individually constrained in the model for each experiment, resulting in values of ~1 day in the high SA case and ~30 days (nearly the entire length of the experimental run) for the medium and low SA cases (**Table 3**).

"Mineral surface" model simulations based on these unique time intervals and a single set of α_{kin} (0.9967) and α_{eq} (1.0000) successfully reproduced fluid $\delta^{30}Si$ trends in all three surface area experiments. Notably, the "mineral surface" transient model captured the full extent of isotopic re-equilibration observed in the high SA experiment including final fluid $\delta^{30}Si$ values significantly more negative than the average bulk composition. This result provides key

740 evidence for the mineral fluid phase isotopically re-equilibrating with the mineral surface
741 rather than the bulk. The values of this isotopically depleted, newly formed mineral surface
742 are explored in further detail below (**Section 4.5**). A major prediction from this transient
743 model is that fluid $\delta^{30}Si$ can re-equilibrate to values distinct from the bulk amorphous silica
744 composition at metastable equilibrium, is validated by this comparison.

745 In the medium and low SA experiments, the apparent kinetic fractionations that were
746 underestimated by the "bulk" model (**Fig. 5C**), are successfully predicted in the transient
747 model. Elevated fluid $\delta^{30}Si$ values observed throughout the duration of these lower surface
748 area experiments are also reproduced and result from slower precipitation kinetics
749 maintaining the systems at far-from equilibrium conditions. Thus, strong consensus between
750 transient "mineral surface" model predictions and our three experiments indicate that reactive
751 surface area (i.e. fluid-mineral interaction depth) and corresponding transient isotope behavior
752 (deriving from the isotopic co-evolution of the fluid and growing amorphous silica surface)
753 has a first order control on $\delta^{30}Si$ fractionation during amorphous silica precipitation.

754 A key component of our transient model is the time interval and its dependence on the
755 reactive surface area. As further detailed in **Section 2.3**, the mass of dissolved silica removed
756 from solution over the given time interval is used as an approximation for the depth into the
757 mineral surface in contact with the surrounding fluid. In our transient framework, fluid $\delta^{30}Si$
758 re-equilibration is dependent on the amount of mineral surface that the fluid can isotopically
759 interact with (which is dictated by the surface area). Thus, the time interval serves as a proxy
760 for the fluid-mineral interaction depth.

761 To further explore this relationship, a sensitivity analysis was conducted on the high SA
762 case where, all other parameters remaining constant, transient simulations were run for three
763 different time intervals: 2.4 hrs, 1 hr, and 10 days (**Fig. 6**). Overall, changing T has no impact
764 on dissolved silica concentrations (**Fig. 6A**). However, fluid $\delta^{30}Si$ does change considerably

765 with varying T (**Fig. 6B**). In the case where T = 2.4 hrs (i.e. the running average is performed
766 on the mass precipitated over the past 2.4 hrs) the fluid interacts and re-equilibrates with a
767 thin portion of the recently formed mineral surface that is largely depleted in ^{30}Si due to the
768 initial period of kinetic fractionation. As a result, fluid $\delta^{30}Si$ after initial kinetic fractionation
769 re-equilibrated to significantly more negative values (-3.32‰ at 35 days). On the other hand,
770 when T is set to 10 days the running average is performed over a greater portion of the
771 mineral surface and thus fluid $\delta^{30}Si$ re-equilibrates towards values considerably closer to the
772 bulk. As is shown in **Fig. 6B**, time intervals of 2.4 hours and 10 days both fail to capture the
773 measured fluid $\delta^{30}Si$ timeseries trend for our high SA case whereas we find good agreement
774 when setting T to 1 day. This sensitivity analysis supports the dependence of the time interval
775 on surface area and its role as a proxy for the fluid-mineral interaction depth, which controls
776 the extent to which the fluid and growing mineral surface can isotopically co-evolve and re-
777 equilibrate.

778 **4.5 Estimating the solid-fluid interaction depth and extent of re-equilibration**

779 ***4.5.1 Numerical approach***

780 A major implication that arises from our transient "mineral surface" model is that the
781 mass of new mineral that the fluid can interact with is now being tracked within the model
782 framework. Thus, we are now poised to explore how the depth into the mineral surface that
783 the fluid exchanges with is dictated by surface area. As a first approximation, we start by
784 calculating the growth rate of accumulating amorphous silica precipitating out of solution
785 using the following expression (**eq. 8;** Rimstidt and Barnes, 1980; Geilert et al., 2014)

786 $$R_G = \left[\frac{N_{SiO_{2(ppt),\,t+1}} - N_{SiO_{2(ppt),\,t}}}{S \cdot \Delta t}\right] * M_v \quad (8)$$

787 where the instantaneous growth rate (R_G) in units of nm/s is determined by the precipitation
788 rate (**eq. 5**) and the molar volume, M_v, of 30 cm^3 mol^{-1}. Through R_G, the amount of new

amorphous silica accumulated onto the seeds, referred to as the "surface growth", can be plotted as a function of time both experimentally and numerically (**Fig. 7**). In general, the accumulated surface thicknesses calculated using the numerical model results increase with time and stabilize as the growth rate decreases in the approach to metastable equilibrium, The results are in close agreement with the experimentally constrained surface thickness accumulation as a function of surface area and the amount of surface-normal growth reported earlier (**Section 4.3**). This observation is also in agreement with the Geilert et al. (2014) amorphous silica precipitation study. Growth of the amorphous silica surface is dependent on the reactive surface area available. For a lower available surface area, the same mass of new mineral formed must achieve a thicker depth at an equivalent point in time. This is reflected in the medium (total accumulated depth = 36.5 nm) and low (total accumulated depth = 58.0 nm) surface area numerical model results, which show significantly more overall surface growth as compared to the high SA case (total accumulated depth = 0.193 nm) despite starting at higher solid:fluid mass ratios. Similarly, the lower available surface area simulation achieves a given depth at an earlier time relative to the medium and high SA cases.

Having confirmed this estimate of total surface growth both experimentally and numerically, we may now track the $\delta^{30}Si$ of both the bulk phase and the net accumulated surface throughout the course of our transient simulations for the three surface area cases (**Fig. 8**). Accurate behavior of the model is verified by checking mass balance. The model tracks the isotope ratio of the entire bulk mass of $SiO_{2(am)}$, including the seed crystals through time, as well as the mass lost from the fluid that was incorporated into the new amorphous silica surface for both isotopes. Using these values, we show that the initial $SiO_{2(am)}$ subtracted from the bulk $SiO_{2(am)}$ at any given timestep perfectly recovers the mass of $SiO_{2(aq)}$ lost from the fluid and the corresponding mass-weighted difference in $\delta^{30}Si$ (**Table 2**), thereby verifying that mass balance is fully adhered to in the model both for concentration

814 and isotope ratio. As a final check, we verify that the mass and isotope ratio of $SiO_{2(aq)}$ and
815 net accumulated $SiO_{2(am)}$ sum to the initial isotope ratio of the fluid at the beginning of the
816 experiment.

817 In these simple, closed system batch reactors, our numerical simulations show good
818 agreement with the experimentally calculated ($\delta^{30}Si_{ppt}$) and measured (bulk $\delta^{30}Si_{(am)}$) values
819 (**Table 2**). However, in a more complex open system, this numerical approach would be our
820 only recourse to estimate such values. Thus, a significant advantage that arises from our
821 transient model is that the net accumulated surface $\delta^{30}Si$ can be estimated numerically by
822 tracking the ^{28}Si and ^{30}Si cumulatively precipitated out of solution over the length of the
823 simulation, representing a component of the overall bulk solid measured directly at the end of
824 the experiment.

825 As a result of the large mass of silica initially contained in the bulk phase seed crystals
826 relative to the fluid, bulk $\delta^{30}Si$ is not appreciably sensitive to precipitation over the duration of
827 the experiment. This is demonstrated both by direct measurement and within the numerical
828 model. In contrast, $\delta^{30}Si$ of the growing mineral surface shifts significantly through time,
829 reflecting both the preferential incorporation of ^{28}Si during the kinetically dominated portion
830 of the experiment and subsequent re-equilibration with the surrounding fluid at later times. In
831 the high SA case (**Fig. 8A**), the reaction is sufficiently rapid to allow the net accumulated
832 $SiO_{2(am)}$ $\delta^{30}Si$ to approach the fluid $\delta^{30}Si$ at metastable equilibrium whereas in the medium
833 (**Fig. 8B**) and low (**Fig. 8C**) surface area cases the net surface remains far from both bulk and
834 fluid values at the end of the experiments.

835 Notably, the numerical model prediction of net accumulated $\delta^{30}Si$ at the end of the high
836 SA experiment predicts a slight turnover where the newly accumulated precipitate values
837 become more elevated than the fluid despite an equilibrium fractionation factor of 1.0. We
838 reassert that this behavior does not violate mass balance (**Table 2**) and can be attributed to the

839 higher-order rate law (**eq. 2**), which impedes complete isotopic equilibration. As discussed
840 earlier, the isotopic solid solution derivation used here (Druhan et al., 2013) is only strictly
841 valid under a linear TST expression in the limit as isotopic equilibrium is acheived.
842 Interestingly, our experimentally calculated net surface $\delta^{30}Si$ based on simple mass balance
843 (**eq. 6**) also show the net surface approaching and then becoming greater than the fluid $\delta^{30}Si$
844 values. Though beyond the scope of the present study, this independent observation agrees
845 with the numerical model and suggests implications for the behavior of isotope exchange at
846 higher order rates near equilibrium. In addition, this strong agreement between our numerical
847 and experimental $\delta^{30}Si_{ppt}$ values indicate that the solid phase became isotopically zoned
848 normal to the mineral surface, particularly in the high SA case. These results build upon and
849 expand previous transient-based models (Druhan et al., 2013; Steefel et al., 2014; Druhan et
850 al., 2015) suggesting that the formation of isotopic heterogeneity (i.e. zoning) within a
851 growing mineral phase imparts a significant influence on observed fluid isotopic values.

852 Having now constrained $\delta^{30}Si$ of the net accumulated surface throughout the course of
853 our transient simulations, we turn to the component of this newly formed mineral that the
854 fluid interacts with through time. For the medium and low SA cases, the depth into the
855 mineral surface that defines the mole fractions (**eq. 4**) is defined by the user-specified time
856 interval (T) and the depth of the accumulated surface thickness tracked through time
857 (calculated above, **eq. 8** and **Fig. 7**). The mineral-fluid interaction depth is then calculated
858 based on the cumulative amount of $SiO_{2(am)}$ precipitated over the given time interval. For
859 these two surface areas, the time interval necessary to accurately recover our observations in
860 the numerical simulations was long (~30 days). This means that the majority of the net
861 accumulated precipitate was included in the solid solution model (**eq. 2**). As a result, these
862 values (**Table 4**) for the medium and low SA cases were 14.3 nm and 27.9 nm, respectively,
863 at the end of the simulation. These values represent 39% and 48% of the total depth of freshly

accumulated $SiO_{2(am)}$ precipitated out of the solution over the 35-day simulation for the medium and low SA cases, respectively. This calculation suggests that early in the reaction, when precipitation rates are highest, the fluid interacts with effectively the entire growing amorphous silica surface. Thus, for these medium and low SA cases, slower precipitation kinetics maintained far from isotopic equilibrium conditions throughout the course of the experiment, offsetting the contribution from the backward reaction (i.e. delaying the onset of isotopic re-equilibration) while also allowing the fluid to interact with a large portion of the newly-formed mineral surface.

For the high SA case, the time interval T necessary to recover our observations was much shorter (1 day). Following the same calculations used above at early time when precipitation rates were rapid, the fluid initially interacts with approximately 1 monomolecular surface layer (depth = 0.095 nm). However, as time proceeds and reaction rates slow down, this short time interval means that the fluid-mineral surface interaction depth becomes very thin as a result of less precipitation onto the newly formed mineral surface. At this late stage of the experiment, the combination of slow precipitation rate (where contributions from isotopic re-equilibration become more substantial), and a small solid phase component defining the mole fractions (**eq. 2**) allows the fluid to shift to substantially lower values. This behavior is complicated by the high order reaction rate, resulting in an inability to perfectly resolve the fluid-mineral interaction depth at near-equilibrium conditions using the selected time interval as a proxy.

To circumvent this limitation, we offer a simple scaling calculation for the high SA case where the original starting solid:fluid mass ratio is increased to the starting solid:fluid mass ratio for the medium and low SA cases. Normalizing to the same solid:fluid mass ratios allows us to directly compare the mass precipitated out of solution over the duration of the three experiments. The result is that the net accumulated mass of $SiO_{2(am)}$ for the normalized

889 high SA case (0.793 mmoles) was 18% and 27% more than the mass accumulated over the
890 same duration in the medium (0.647 mmoles) and low (0.582 mmoles) SA experiments,
891 respectively. However, the depth of this new mineral growth calculated for the high SA case
892 using this scaling approach (0.108 nm) is smaller than the medium and low SA interaction
893 depths as a result of the correspondingly scaled high surface area (SSA_{init} = 216 m^2). These
894 results suggest that the original seed crystal isotopic ratio is much less isolated from the
895 surrounding fluid in the high SA case, and that only a very small veneer of new precipitate
896 with correspondingly negative values is available to include in the mole fraction calculation
897 (**eq. 4**). This difference is consistent with the observation of rapid turnover in the fluid $\delta^{30}Si$
898 towards values, which approach, and ultimately become more negative, than the bulk.
899 A significant implication arising from these simulations is that isotopic re-
900 equilibration can exert a large influence on the overall $\delta^{30}Si$ value of a newly formed
901 amorphous silica surface (**Fig. 8A**). Our model is constructed such that over a given time
902 interval, a higher precipitation rate will result in a larger mass included in the definition of the
903 mole fractions used to calculate the corresponding evolution of the fluid isotope ratio (**eq. 2,**
904 **4**). This means that at rapid mineral growth rates, a larger component of the new mineral
905 phase is interacting with the fluid. As the growth rate slows, this fraction of the total new
906 precipitate diminishes, suggesting that in the approach to equilibrium the ability of the fluid to
907 alter the solid isotope ratio also diminishes. Though this behavior is imposed through our
908 model framework, we have demonstrated that the approach accurately recovers the behavior
909 of the co-evolving fluid and solid surfaces across a variety of growth rates and surface areas.
910 Thus, according to our transient model simulations, the rate at which stable isotopic re-
911 equilibration can occur during secondary amorphous silica formation is a balance between the
912 amount of newly formed solid available to interact with the fluid and the proximity to
913 equilibrium. What re-equilibration is able to occur can be accomplished relatively quickly (~1

914 month) and can involve a large portion of the newly formed solid. This finding is in contrast
915 to stable mineral recrystallization results of foraminiferal tests, which observe only ~5%
916 recrystallization over 100 days (Chanda et al., 2019), though our results are unique to the
917 (paleo)environmental δ^{30}Si signatures within secondary amorphous silica solids.

918 ***4.5.2 Isotope mass balance approach***

919 The extent to which these isotopic signatures of mineral growth are reset is fundamental
920 to the fidelity of geochemical and paleoclimatology/paleoceanography proxies used to infer
921 modern and ancient environments. Several recrystallization models have been proposed in the
922 literature to quantify the magnitudes and rates of stable mineral recrystallization, including
923 the frequently employed "fractional approach" model based on mole fractions of the solid and
924 fluid phases (summarized by Gorski and Fantle, 2017) or simple isotope mass balance models
925 like those developed by Mavromatis et al.(2016, 2017) that generally take the form of (**eq. 9**):

926 $$\delta_{fluid,eq} = \delta_{fluid}\left(1 - f_{solid}\right) + \delta_{solid} \times f_{solid} \qquad (9)$$

927 where the fraction of the fluid phase concentration that derives from exchange with the solid
928 phase (f_{solid}) is dependent on the isotopic ratio of the fluid at equilibrium ($\delta_{fluid,eq}$), the isotopic
929 composition of the fluid at the end of the precipitation event (δ_{fluid}), and the isotopic
930 composition of the solid phase (δ_{solid}). This approach requires information regarding the
931 crystal structure, specifically the geometry of the unit cell and how the particles are arranged
932 within a given unit cell, in order to estimate the concentration of the given element of interest
933 in the outer surface layer (necessary for quantifying exchange between the solid and fluid
934 phases).

935 As an independent constraint, we applied these calculations for our amorphous silica
936 precipitation data (**see Appendix C**). Fluid interaction depth values obtained using the
937 Mavromatis et al. (2016, 2017) model were similar to our transient-based estimations, but
938 systematically returned slightly higher values. For the medium and low SA cases their

approach suggests that as much as 60% of the total new precipitate is still interacting with the fluid in comparison to our prior estimates of 39% and 48%, respectively (**Table 4**). Given the differences in the two approaches, this level of agreement suggests our approach is robust. Two sources of discrepancy may contribute to the differences in these methods for calculating the fluid-solid interaction depth. The first resides in the unit cell geometry approximation, which in this case was not available for amorphous silica explicitly and so had to be approximated by a rhombohedral unit cell used for quartz (V = 113 Å, edge length 5.405 Å) where there are ~ 3atoms Si/ unit cell (**Fig. C.1**). The second limitation arises from fluid interaction depth calculations using simplified closed-system isotopic mass balance equations (e.g., **eq. 9**) where steady state assumptions have to be made. As shown earlier in this study, such assumptions are incorrect based on our transient model results and thus yield inaccurate interpretations. These limitations highlight potential advantages in using the transient model approach to constrain the fluid-solid interaction and re-equilibration depth: (1) there is no need to use crystal structure geometries and other parameters to approximate outer surface layer elemental concentrations; (2) the isotopic composition of the component of the surface directly interacting with the fluid can be directly tracked. This tracking is particularly effective for cases where rates adhere to linear TST rate laws and/or express slower overall kinetics.

4.6 Implications for silicate weathering proxies

Our experiments and transient models indicate that the observed fractionation factors during secondary amorphous silica formation are surface area dependent, and that this dependence is more nuanced than simply a scaling of the reaction rate. This relationship could have important implications for other commonly formed secondary minerals. Average observed fractionation factors produced in this study ($\varepsilon_{am.silica-SiO2(aq)}$ = -2.5‰) are generally higher than what is observed for clays (ε = -1.5‰, Frings et al., 2016) or for

amorphous silica precipitation in flow throw experiments (ε = -2.10‰, Geilert et al., 2014), but are consistent with ε observed for previous batch amorphous silica precipitation studies: ε = -3.4‰ (am.silica batch experiments, Roerdink et al.,2015) and ε = -3.9‰ (biogenic opal precipitation, Ziegler et al., 2005). Despite conducting our amorphous silica precipitation experiments at dissolved SiO_2 concentrations higher than what is traditionally observed in natural weathering environments (Dürr et al., 2011; Opfergelt and Delmelle, 2012; Patrick J Frings et al., 2016; Poitrasson, 2017), the results from this study can be extendable to secondary silica proxies in natural weathering environments where the rate of mineral formation and, thus, the timing and extent of isotope re-equilibration could potentially exhibit a similar dependence on surface area.

For example, findings from our study could help explain the paradox of uniformly low $\delta^{30}Si$ signatures in secondary clays within weathering environments (ranging between -2.95 to -0.16‰ (Poitrasson, 2017)) and correspondingly high $\delta^{30}Si$ in soil waters (Ziegler et al., 2005; Opfergelt et al., 2010; Opfergelt and Delmelle, 2012), despite estimated equilibrium fractionation greater than 1.0 for secondary clays (Méheut et al., 2007). Secondary clays in low temperature environments typically form through conversion of high surface area aluminum oxide precursors, like allophane and gibbsite, towards more stable crystalline, lower surface area clays like kaolinite (i.e. low temperature silica diagenesis). Oelze et al.(2014) showed that Si adsorption onto gibbsite yields a significant kinetic fractionation and proposed that these large kinetic signatures are preserved due to their quick conversion to secondary clays. This explanation is supported by our transient framework in that lower surface area grains minimize the extent of isotopic exchange and thus preserve kinetic signatures in both fluid and secondary mineral phases for significantly long periods of time.

The results of this study can also be extended to iron oxide formation, another commonly formed secondary phase in natural environments, where, for instance, the extent of stable

isotope exchange between dissolved Fe(II) and Fe(III) in hematite was found be greater in grains of smaller particle size, or higher reactive surface area (Frierdich et al., 2015). Ultimately, to better interpret isotope fractionation during secondary mineral formation in weathering environments, a transient approach that considers the physical characteristics of the solid phase is required. Our transient model, then, represents a new generation of isotope fractionation models that can be applied to many different systems to better predict observed fractionation factors in natural settings and quantify the extent to which these signatures are preserved in the surrounding porous media.

5. SUMMARY AND CONCLUSIONS

This study reports **(1)** δ^{30}Si isotopic fractionation during amorphous silica precipitation "free-drift" experiments conducted over a range of surface areas at ambient temperatures (20℃) and near-neutral pH (~7.3) ; (**2**) the development and application of a transient-based numerical model for simulating isotopic fractionation between interacting minerals and fluids in dynamic, open systems characterizing weathering environments; and (**3**) a novel approach for tracking isotopic zoning in minerals using a time interval to perform a running average of the newly precipitated mineral surface isotopic composition in contact with the surrounding fluid. Our main findings can be summarized as follows:

(1) Surface area exerts a first order control on δ^{30}Si re-equilibration during secondary amorphous silica precipitation. Fluids interacting with mineral grains of high surface area will isotopically re-equilibrate over short timescales (days to weeks) whereas interaction with grains of reasonably lower surface areas will preserve the kinetic isotopic signature over longer periods of time. This study provides further evidence that fluid – mineral interactions do have the capacity to alter isotope archives recorded in geochemical proxies under specific conditions.

(2) The extent to which isotopic re-equilibration significantly alters the overall kinetic isotopic signature of newly formed secondary minerals is dependent on the fluid- surface interaction depth, which is in turn a function of the mass precipitated and the surface area. In the case of amorphous silica formation, isotopic re-equilibration is a balance between the portion of the total accumulated mineral surface interacting with the fluid and the extent to which growth rates are sufficiently slow to impede the influence of the back reaction. In this sense, low surface areas seem to protect or preserve secondary solid phase isotopic signatures.

(3) Finally, in application to modern weathering environments, our results show that variability in observed fractionation factors generated in open, transient systems could have a dependence on both surface area and solid:fluid mass ratios. Thus, at the continuum scale, metrics for the isotopic composition of the evolving mineral surface are required for accurate interpretations of observed isotopic signatures used for characterizing environmental conditions of mineral formation. In this regard, a transient approach is necessary to characterize mineral isotopic heterogeneity.

ACKNOWLEDGMENTS

This material is based upon work supported by the National Science Foundation Graduate Research Fellowship Program under Grant No. DGE -1144245 and by the Chateaubriand Fellowship of the Office for Science & Technology of the Embassy of France in the United States. Special acknowledgment is given to Jérôme Gaillardet, Julien Bouchez, and the G2E (Géochimie des enveloppes externs) group for their assistance and allowing us access to the facilities at the Ínstitut de Physique du Globe de Paris (IPGP) in Paris, France to perform measurements necessary for this study. We are thankful to Jessica Dallas and Pascale Louvat for their support with silicon isotopic analyses and Pierre Burckel for silica concentration analyses.

REFERENCES

Aagaard P. and Helgeson H. C. (1982) Thermodynamic and kinetic constraints on reaction rates among minerals and aqueous solutions. I. Theoretical considerations. *Am. J. Sci.* **282**, 237–285.

Alfredsson H., Hugelius G., Clymans W., Stadmark J., Kuhry P. and Conley D. J. (2015) Amorphous silica pools in permafrost soils of the Central Canadian Arctic and the potential impact of climate change. *Biogeochemistry* **124**, 441–459. Available at: https://link-springer-com /article/10.1007/s10533-015-0108-1.

Basile-Doelsch I., Meunier J. D. and Parron C. (2005) Another continental pool in the terrestrial silicon cycle. *Nature* **433**, 399–402. Available at: http://www.nature.com /nature/journal/v433/n7024/full/nature03217.html?foxtrotcallback=true.

Van Den Boorn S. H. J. M., Vroon P. Z., Van Belle C. C., Van Der Wagt B., Schwieters J. and Van Bergen M. J. (2006) Determination of silicon isotope ratios in silicate materials by high-resolution MC-ICP-MS using a sodium hydroxide sample digestion method. *J. Anal. At. Spectrom.* **21**, 734–742. Available at: http://xlink.rsc.org/?DOI=b600933f.

Bouchez J., Blanckenburg F. von and Schuessler J. A. (2013) Modeling novel stable isotope ratios in the weathering zone. *Am. J. Sci.* **313**, 267–308. Available at: http://www.ajsonline.org/content/313/4/267.

Chanda P., Gorski C. A., Oakes R. L. and Fantle M. S. (2019) Low temperature stable mineral recrystallization of foraminiferal tests and implications for the fidelity of geochemical proxies. *Earth Planet. Sci. Lett.* **506**, 428–440. Available at: https://www.sciencedirect.com/science/article/pii/S0012821X18306629?via%3Dihub.

Curti E., Fujiwara K., Iijima K., Tits J., Cuesta C., Kitamura A., Glaus M. A. and Müller W. (2010) Radium uptake during barite recrystallization at 23 ± 2 °C as a function of

1065 solution composition: An experimental 133Ba and 226Ra tracer study. *Geochim.*
1066 *Cosmochim. Acta* **74**, 3553–3570. Available at:
1067 http://www.sciencedirect.com/science/article/pii/S0016703710001456.
1068 Curti E., Kulik D. A. and Tits J. (2005) Solid solutions of trace Eu(III) in calcite:
1069 Thermodynamic evaluation of experimental data over a wide range of pH and pCO2.
1070 *Geochim. Cosmochim. Acta* **69**, 1721–1737. Available at:
1071 https://www.sciencedirect.com/science/article/pii/S0016703704004910.
1072 Delstanche S., Opfergelt S., Cardinal D., Elsass F., André L. and Delvaux B. (2009) Silicon
1073 isotopic fractionation during adsorption of aqueous monosilicic acid onto iron oxide.
1074 *Geochim. Cosmochim. Acta* **73**, 923–934. Available at:
1075 https://www.sciencedirect.com/science/article/pii/S0016703708006832?via%3Dihub.
1076 DePaolo D. J. (2004) Calcium Isotopic Variations Produced by Biological, Kinetic,
1077 Radiogenic and Nucleosynthetic Processes. *Rev. Mineral. Geochemistry* **55**, 255–288.
1078 Available at:
1079 https://pubs.geoscienceworld.org/msa/rimg/article/55/1/255/87511/calcium-isotopic-
1080 variations-produced-by-biological.
1081 DePaolo D. J. (2011) Surface kinetic model for isotopic and trace element fractionation
1082 during precipitation of calcite from aqueous solutions. *Geochim. Cosmochim. Acta* **75**,
1083 1039–1056. Available at: http://doi.org/10.1016/j.gca.2010.11.020.
1084 Druhan J. L., Brown S. T. and Huber C. (2015) Isotopic Gradients Across Fluid–Mineral
1085 Boundaries. *Rev. Mineral. Geochemistry* **80**, 355–391. Available at:
1086 http://rimg.geoscienceworld.org/content/80/1/355.
1087 Druhan J. L., Steefel C. I., Williams K. H. and DePaolo D. J. (2013) Calcium isotope
1088 fractionation in groundwater: Molecular scale processes influencing field scale behavior.
1089 *Geochim. Cosmochim. Acta* **119**, 93–116. Available at:

https://www.sciencedirect.com/science/article/pii/S0016703713003098?via%3Dihub.

Dupuis R., Benoit M., Nardin E. and Méheut M. (2015) Fractionation of silicon isotopes in liquids: The importance of configurational disorder. *Chem. Geol.* **396**, 239–254. Available at: http://files/3/Dupuis et al., 2015.pdf.

Enüstün B. V. and Turkevich J. (1960) Solubility of Fine Particles of Strontium Sulfate. *J. Am. Chem. Soc.* **82**, 4502–4509. Available at: http://pubs.acs.org/doi/abs/10.1021/ja01502a015 [Accessed February 7, 2019].

Fantle M. S. (2015) Calcium isotopic evidence for rapid recrystallization of bulk marine carbonates and implications for geochemical proxies. *Geochim. Cosmochim. Acta* **148**, 378–401. Available at: https://doi.org/10.1016/j.gca.2014.10.005.

Fantle M. S. (2010) Evaluating the Ca Isotope Proxy. *Am. J. Sci.* **310**, 194–230. Available at: https://doi.org/10.2475/03.2010.03.

Fantle M. S. and DePaolo D. J. (2007) Ca isotopes in carbonate sediment and pore fluid from ODP Site 807A: The Ca2+(aq)–calcite equilibrium fractionation factor and calcite recrystallization rates in Pleistocene sediments. *Geochim. Cosmochim. Acta* **71**, 2524–2546. Available at: https://doi.org/10.1016/j.gca.2007.03.006.

Fleming B. A. (1986) Kinetics of reaction between silicic acid and amorphous silica surfaces in NaCl solutions. *J. Colloid Interface Sci.* **110**, 40–64. Available at: http://www.sciencedirect.com/science/article/pii/0021979786903516.

Frierdich A. J., Beard B. L., Thiruchelvi R. R., Scherer M. M. and Johnson C. M. (2014) Iron isotope fractionation between aqueous Fe(II) and goethite revisited: New insights based on a multi-direction approach to equilibrium and isotopic exchange rate modification. *Geochim. Cosmochim. Acta* **139**, 383–398. Available at: https://doi.org/10.1016/j.gca.2014.05.001.

Frierdich A. J., Helgeson M., Liu C., Wang C., Rosso K. M. and Scherer M. M. (2015) Iron

1115 Atom Exchange between Hematite and Aqueous Fe(II). *Environ. Sci. Technol.* **49**, 8479–
1116 8486. Available at: http://files/146/Frierdich et al., 2015.pdf.
1117 Frings Patrick J., Clymans W., Fontorbe G., De La Rocha C. L. and Conley D. J. (2016) The
1118 continental Si cycle and its impact on the ocean Si isotope budget. *Chem. Geol.* **425**, 12–
1119 36. Available at:
1120 https://www.sciencedirect.com/science/article/pii/S0009254116300201?via%3Dihub.
1121 Frings Patrick J, Clymans W., Fontorbe G., De La Rocha C. L. and Conley D. J. (2016) The
1122 continental Si cycle and its impact on the ocean Si isotope budget. *Chem. Geol.* **425**, 12–
1123 36. Available at: http://www.sciencedirect.com/science/article/pii/S0009254116300201.
1124 Geilert S., Vroon P. Z., Keller N. S., Gudbrandsson S., Stefánsson A. and van Bergen M. J.
1125 (2015) Silicon isotope fractionation during silica precipitation from hot-spring waters:
1126 Evidence from the Geysir geothermal field, Iceland. *Geochim. Cosmochim. Acta* **164**,
1127 403–427. Available at:
1128 http://www.sciencedirect.com/science/article/pii/S0016703715003804.
1129 Geilert S., Vroon P. Z., Roerdink D. L., Van Cappellen P. and van Bergen M. J. (2014)
1130 Silicon isotope fractionation during abiotic silica precipitation at low temperatures:
1131 Inferences from flow-through experiments. *Geochim. Cosmochim. Acta* **142**, 95–114.
1132 Available at: https://doi.org/10.1016/j.gca.2014.07.003.
1133 Georg R.B., Reynolds B. C., Frank M. and Halliday A. N. (2006) Mechanisms controlling the
1134 silicon isotopic compositions of river waters. *Earth Planet. Sci. Lett.* **249**, 290–306.
1135 Available at:
1136 https://www.sciencedirect.com/science/article/pii/S0012821X06004973?via%3Dihub.
1137 Georg R B, Reynolds B. C., Frank M. and Halliday A. N. (2006) New sample preparation
1138 techniques for the determination of Si isotopic compositions using MC-ICPMS. *Chem.*
1139 *Geol.* **235**, 95–104. Available at: https://doi.org/10.1016/j.chemgeo.2006.06.006.

1140 Georg R.B., Reynolds B. C., West A. J., Burton K. W. and Halliday A. N. (2007) Silicon
1141 isotope variations accompanying basalt weathering in Iceland. *Earth Planet. Sci. Lett.*
1142 **261**, 476–490. Available at:
1143 https://www.sciencedirect.com/science/article/pii/S0012821X07004530?via%3Dihub.
1144 Georg R B, Reynolds B. C., West A. J., Burton K. W. and Halliday A. N. (2007) Silicon
1145 isotope variations accompanying basalt weathering in Iceland. *Earth Planet. Sci. Lett.*
1146 **261**, 476–490. Available at: https://doi.org/10.1016/j.epsl.2007.07.004.
1147 Georg R. B., Zhu C., Reynolds B. C. and Halliday A. N. (2009) Stable silicon isotopes of
1148 groundwater, feldspars, and clay coatings in the Navajo Sandstone aquifer, Black Mesa,
1149 Arizona, USA. *Geochim. Cosmochim. Acta* **73**, 2229–2241. Available at:
1150 https://doi.org/10.1016/j.gca.2009.02.005.
1151 Gorski C. A. and Fantle M. S. (2017) Stable mineral recrystallization in low temperature
1152 aqueous systems: A critical review. *Geochim. Cosmochim. Acta* **198**, 439–465. Available
1153 at: https://www.sciencedirect.com/science/article/pii/S0016703716306500?via%3Dihub.
1154 Gunnarsson I. and Anórsson S. (2000) Amorphous silica solubility and the thermodynamic
1155 properties of H4SiO°4 in the range of 0° to 350°C at Psat. *Geochim. Cosmochim. Acta*
1156 **64**, 2295–2307. Available at: https://doi.org/10.1016/S0016-7037(99)00426-3.
1157 Halbach P. and Puteanus D. (1984) The influence of the carbonate dissolution rate on the
1158 growth and composition of Co-rich ferromanganese crusts from Central Pacific
1159 seamount areas. *Earth Planet. Sci. Lett.* **68**, 73–87. Available at:
1160 https://www.sciencedirect.com/science/article/pii/0012821X84901419?via%3Dihub.
1161 Handler R. M., Beard B. L., Johnson C. M. and Scherer M. M. (2009) Atom Exchange
1162 between Aqueous Fe(II) and Goethite: An Fe Isotope Tracer Study. *Environ. Sci.*
1163 *Technol.* **43**, 1102–1107. Available at: http://files/32/Handler et al.,2009.pdf.
1164 Handler R. M., Frierdich A. J., Johnson C. M., Rosso K. M., Beard B. L., Wang C., Latta D.

E., Neumann A., Pasakarnis T., Premaratne W. A. P. J. and Scherer M. M. (2014) Fe(II)-Catalyzed Recrystallization of Goethite Revisited. *Environ. Sci. Technol.* **48**, 11302–11311. Available at: http://pubs.acs.org/doi/10.1021/es503084u.

He H., Zhang S., Zhu C. and Liu Y. (2015) Equilibrium and kinetic Si isotope fractionation factors and their implications for Si isotope distributions in the Earth's surface environments. *Acta Geochim.* **35**, 15–24. Available at: http://link.springer.com/article/10.1007/s11631-015-0079-x.

Helgeson H. C., Murphy W. M. and Aagaard P. (1984) Thermodynamic and kinetic constraints on reaction rates among minerals and aqueous solutions. II. Rate constants, effective surface area, and the hydrolysis of feldspar. *Geochim. Cosmochim. Acta* **48**, 2405–2432. Available at: http://www.sciencedirect.com/science/article/pii/0016703784902941.

Hofmann A. E., Bourg I. C. and DePaolo D. J. (2012) Ion desolvation as a mechanism for kinetic isotope fractionation in aqueous systems. *Proc. Natl. Acad. Sci.* **109**, 18689–18694. Available at: https://www.pnas.org/content/109/46/18689.

Holdren G. R. and Speyer P. M. (1985) Reaction rate-surface area relationships during the early stages of weathering-I. Initial observations. *Geochim. Cosmochim. Acta* **49**, 675–681. Available at: https://www.sciencedirect.com/science/article/pii/0016703785901620.

Huber C., Druhan J. L. and Fantle M. S. (2017) Perspectives on geochemical proxies: The impact of model and parameter selection on the quantification of carbonate recrystallization rates. *Geochim. Cosmochim. Acta* **217**, 171–192. Available at: http://www.sciencedirect.com/science/article/pii/S0016703717305045.

Hughes H. J., Sondag F., Santos R. V, André L. and Cardinal D. (2013) The riverine silicon isotope composition of the Amazon Basin. *Geochim. Cosmochim. Acta* **121**, 637–651. Available at: http://www.sciencedirect.com/science/article/pii/S0016703713004304.

1190 Iler R. K. (1979) *The Chemistry of Silica: Solubility, Polymerization, Colloid and Surface*
1191 *Chemistry, and Biochemistry*., John Wiley & Sons.
1192 Inskeep W. P. and Bloom P. R. (1985) An evaluation of rate equations for calcite
1193 precipitation kinetics at pCO2 less than 0.01 atm and pH greater than 8. *Geochim.*
1194 *Cosmochim. Acta* **49**, 2165–2180. Available at:
1195 http://www.sciencedirect.com/science/article/pii/0016703785900742.
1196 Jacobson A. D., Grace Andrews M., Lehn G. O. and Holmden C. (2015) Silicate versus
1197 carbonate weathering in Iceland: New insights from Ca isotopes. *Earth Planet. Sci. Lett.*
1198 **416**, 132–142. Available at:
1199 http://www.sciencedirect.com/science/article/pii/S0012821X15000576.
1200 Johnson C. M., Skulan J. L., Beard B. L., Sun H., Nealson K. H. and Braterman P. S. (2002)
1201 Isotopic fractionation between Fe(III) and Fe(II) in aqueous solutions. *Earth Planet. Sci.*
1202 *Lett.* **195**, 141–153. Available at: https://doi.org/10.1016/S0012-821X(01)00581-7.
1203 Joshi P., Fantle M. S., Larese-Casanova P. and Gorski C. A. (2017) Susceptibility of Goethite
1204 to Fe 2+-Catalyzed Recrystallization over Time. Available at:
1205 https://pubs.acs.org/doi/10.1021/acs.est.7b02603?mobileUi=0.
1206 Keir R. S. (1980) The dissolution kinetics of biogenic calcium carbonates in seawater.
1207 *Geochim. Cosmochim. Acta* **44**, 241–252. Available at:
1208 https://www.sciencedirect.com/science/article/pii/0016703780901350?via%3Dihub.
1209 Kiczka M., Wiederhold J. G., Frommer J., Kraemer S. M., Bourdon B. and Kretzschmar R.
1210 (2010) Iron isotope fractionation during proton- and ligand-promoted dissolution of
1211 primary phyllosilicates. *Geochim. Cosmochim. Acta* **74**, 3112–3128. Available at:
1212 https://www.sciencedirect.com/science/article/pii/S0016703710000888?via%3Dihub.
1213 De La Rocha C. L., Brzezinski M. A., DeNiro M. J. and Shemesh A. (1998) Silicon-isotope
1214 composition of diatoms as an indicator of past oceanic change. *Nature* **395**, 680–683.

1215 Available at: http://www.nature.com/articles/27174.
1216 Landrot G., Ajo-Franklin J. B., Yang L., Cabrini S. and Steefel C. I. (2012) Measurement of
1217 accessible reactive surface area in a sandstone, with application to CO2 mineralization.
1218 *Chem. Geol.* **318–319**, 113–125. Available at:
1219 https://www.sciencedirect.com/science/article/pii/S000925411200229X.
1220 Lemarchand D. and Gaillardet J. (2006) Transient features of the erosion of shales in the
1221 Mackenzie basin (Canada), evidences from boron isotopes. *Earth Planet. Sci. Lett.* **245**,
1222 174–189. Available at:
1223 http://www.sciencedirect.com/science/article/pii/S0012821X06001075.
1224 Loretta Ann Williams (2), George A. L. A., Parks G. A. and Crerar D. A. (1985) Silica
1225 Diagenesis, I. Solubility Controls. *SEPM J. Sediment. Res.* **Vol. 55**, 301–311. Available
1226 at: https://pubs.geoscienceworld.org/jsedres/article/55/3/301-311/97760.
1227 Loucaide S., Cappelle P. Van and Behrends T. (2008) Dissolution of biogenic silica from land
1228 to ocean: Role of salinity and pH. *Limnol. Oceanogr.* **53**, 1614–1621. Available at:
1229 http://onlinelibrary.wiley.com/doi/10.4319/lo.2008.53.4.1614/abstract.
1230 Maher K., Steefel C. I., DePaolo D. J. and Viani B. E. (2006) The mineral dissolution rate
1231 conundrum: Insights from reactive transport modeling of U isotopes and pore fluid
1232 chemistry in marine sediments. *Geochim. Cosmochim. Acta* **70**, 337–363. Available at:
1233 http://www.sciencedirect.com/science/article/pii/S0016703705007623.
1234 Maher K., Steefel C. I., White A. F. and Stonestrom D. A. (2009) The role of reaction affinity
1235 and secondary minerals in regulating chemical weathering rates at the Santa Cruz Soil
1236 Chronosequence, California. *Geochim. Cosmochim. Acta* **73**, 2804–2831. Available at:
1237 http://www.sciencedirect.com/science/article/pii/S0016703709000775.
1238 Mavromatis V., Bundeleva I. A., Shirokova L. S., Millo C., Pokrovksy O. S., Bénézeth P.,
1239 Ader M. and Oelkers E. H. (2015) The continuous re-equilibration of carbon isotope

compositions of hydrous Mg carbonates in the presence of cyanobacteria. *Chem. Geol.* **404**, 41–51. Available at: https://doi.org/10.1016/j.chemgeo.2015.03.016.

Mavromatis V., Harrison A. L., Eisenhauer A. and Dietzel M. (2017) Strontium isotope fractionation during strontianite (SrCO3) dissolution, precipitation and at equilibrium. *Geochim. Cosmochim. Acta* **218**, 201–214. Available at: http://www.sciencedirect.com/science/article/pii/S0016703717305410.

Mavromatis V., Pearce C. R., Shirokova L. S., Bundeleva I. A., Pokrovksy O. S., Benezeth P. and Oelkers E. H. (2012) Magnesium isotope fractionation during hydrous magnesium carbonate precipitation with and without cyanobacteria. *Geochim. Cosmochim. Acta* **76**, 161–174. Available at: https://doi.org/10.1016/j.gca.2011.10.019.

Mavromatis V., van Zuilen K., Purgstaller B., Baldermann A., Nägler T. F. and Dietzel M. (2016) Barium isotope fractionation during witherite (BaCO3) dissolution, precipitation and at equilibrium. *Geochim. Cosmochim. Acta* **190**, 72–84. Available at: http://www.sciencedirect.com/science/article/pii/S0016703716303544.

Méheut M., Lazzeri M., Balan E. and Mauri F. (2007) Equilibrium isotopic fractionation in the kaolinite, quartz, water system: Prediction from first-principles density-functional theory. *Geochim. Cosmochim. Acta* **71**, 3170–3181. Available at: https://www.sciencedirect.com/science/article/pii/S0016703707001858.

Méheut M. and Schauble E. A. (2014) Silicon isotope fractionation in silicate minerals: Insights from first-principles models of phyllosilicates, albite and pyrope. *Geochim. Cosmochim. Acta* **134**, 137–154. Available at: http://www.sciencedirect.com/science/article/pii/S0016703714001021.

Morse J. W., Arvidson R. S. and Lüttge A. (2007) Calcium Carbonate Formation and Dissolution. *Chem. Rev.* **107**, 342–381. Available at: http://dx.doi.org/10.1021/cr050358j.

1265 Murphy W. M., Oelkers E. H. and Lichtner P. C. (1989) Surface reaction versus diffusion
1266 control of mineral dissolution and growth rates in geochemical processes. *Chem. Geol.*
1267 **78**, 357–380. Available at: https://doi.org/10.1016/0009-2541(89)90069-7.
1268 Nancollas G. H. and Reddy M. M. (1971) The crystallization of calcium carbonate. II. Calcite
1269 growth mechanism. *J. Colloid Interface Sci.* **37**, 824–830. Available at:
1270 http://www.sciencedirect.com/science/article/pii/0021979771903638.
1271 Oelkers E. H., Berninger U.-N., Pérez-Fernàndez A., Chmeleff J. and Mavromatis V. (2018)
1272 The temporal evolution of magnesium isotope fractionation during hydromagnesite
1273 dissolution, precipitation, and at equilibrium. *Geochim. Cosmochim. Acta* **226**, 36–49.
1274 Available at: http://www.sciencedirect.com/science/article/pii/S0016703717307135.
1275 Oelze M., von Blanckenburg F., Bouchez J., Hoellen D. and Dietzel M. (2015) The effect of
1276 Al on Si isotope fractionation investigated by silica precipitation experiments. *Chem.*
1277 *Geol.* **397**, 94–105. Available at:
1278 http://www.sciencedirect.com/science/article/pii/S0009254115000078.
1279 Oelze M., von Blanckenburg F., Hoellen D., Dietzel M. and Bouchez J. (2014) Si stable
1280 isotope fractionation during adsorption and the competition between kinetic and
1281 equilibrium isotope fractionation: Implications for weathering systems. *Chem. Geol.* **380**,
1282 161–171. Available at: https://doi.org/10.1016/j.chemgeo.2014.04.027.
1283 Opfergelt S., Cardinal D., André L., Delvigne C., Bremond L. and Delvaux B. (2010)
1284 Variations of δ30Si and Ge/Si with weathering and biogenic input in tropical basaltic ash
1285 soils under monoculture. *Geochim. Cosmochim. Acta* **74**, 225–240. Available at:
1286 https://www.sciencedirect.com/science/article/pii/S0016703709006036?via%3Dihub.
1287 Opfergelt S. and Delmelle P. (2012) Silicon isotopes and continental weathering processes:
1288 Assessing controls on Si transfer to the ocean. *Comptes Rendus Geosci.* **344**, 723–738.
1289 Available at: http://www.sciencedirect.com/science/article/pii/S1631071312001605.

1290 Parks G. A. (1984) *SURFACE AND INTERFACIAL FREE ENERGIES OF QUARTZ.*,
1291 Available at:
1292 https://agupubs.onlinelibrary.wiley.com/doi/pdf/10.1029/JB089iB06p03997.
1293 Pearce C. R., Saldi G. D., Schott J. and Oelkers E. H. (2012) Isotopic fractionation during
1294 congruent dissolution, precipitation and at equilibrium: Evidence from Mg isotopes.
1295 *Geochim. Cosmochim. Acta* **92**, 170–183. Available at:
1296 https://doi.org/10.1016/j.gca.2012.05.045.
1297 Peters C. A. (2009) Accessibilities of reactive minerals in consolidated sedimentary rock: An
1298 imaging study of three sandstones. *Chem. Geol.* **265**, 198–208. Available at:
1299 https://www.sciencedirect.com/science/article/pii/S0009254108005299.
1300 Pogge von Strandmann P. A. E., Burton K. W., James R. H., van Calsteren P., Gislason S. R.
1301 and Sigfússon B. (2008) The influence of weathering processes on riverine magnesium
1302 isotopes in a basaltic terrain. *Earth Planet. Sci. Lett.* **276**, 187–197. Available at:
1303 http://www.sciencedirect.com/science/article/pii/S0012821X08006274.
1304 Pogge von Strandmann P. A. E., Opfergelt S., Lai Y.-J., Sigfússon B., Gislason S. R. and
1305 Burton K. W. (2012) Lithium, magnesium and silicon isotope behaviour accompanying
1306 weathering in a basaltic soil and pore water profile in Iceland. *Earth Planet. Sci. Lett.*
1307 **339**–**340**, 11–23. Available at:
1308 http://www.sciencedirect.com/science/article/pii/S0012821X12002658.
1309 Poitrasson F. (2017) Silicon Isotope Geochemistry. *Rev. Mineral. Geochemistry* **82**, 289–344.
1310 Available at: https://pubs.geoscienceworld.org/rimg/article/82/1/289-344/302235.
1311 Pokrovsky O. S., Reynolds B. C., Prokushkin A. S., Schott J. and Viers J. (2013) Silicon
1312 isotope variations in Central Siberian rivers during basalt weathering in permafrost-
1313 dominated larch forests. *Chem. Geol.* **355**, 103–116. Available at:
1314 http://www.sciencedirect.com/science/article/pii/S000925411300329X.

1315 Pringle E. A., Moynier F., Savage P. S., Badro J. and Barrat J.-A. (2014) Silicon isotopes in
1316 angrites and volatile loss in planetesimals. *Proc. Natl. Acad. Sci.* **111**, 17029–17032.
1317 Available at: http://www.pnas.org/content/111/48/17029.
1318 Rayleigh L. (1902) On the distillation of binary mixtures. *Phil. Mag.* **4**, 521–537.
1319 Reynolds B. (2012) Silicon Isotopes as Tracers of Terrestrial Processes. In *Handbook of*
1320 *Environmental Isotope Geochemistry* Advances in Isotope Geochemistry. Springer,
1321 Berlin, Heidelberg. pp. 87–104. Available at:
1322 https://link.springer.com/chapter/10.1007/978-3-642-10637-8_6.
1323 Rimstidt J. D. and Barnes H. L. (1980) The kinetics of silica-water reactions. *Geochim.*
1324 *Cosmochim. Acta* **44**, 1683–1699. Available at:
1325 http://www.sciencedirect.com/science/article/pii/0016703780902203.
1326 Roerdink D. L., van den Boorn S. H. J. M., Geilert S., Vroon P. Z. and van Bergen M. J.
1327 (2015) Experimental constraints on kinetic and equilibrium silicon isotope fractionation
1328 during the formation of non-biogenic chert deposits. *Chem. Geol.* **402**, 40–51. Available
1329 at: http://www.sciencedirect.com/science/article/pii/S0009254115001205.
1330 Skulan J. L., Beard B. L. and Johnson C. M. (2002) Kinetic and equilibrium Fe isotope
1331 fractionation between aqueous Fe(III) and hematite. *Geochim. Cosmochim. Acta* **66**,
1332 2995–3015. Available at: https://doi.org/10.1016/S0016-7037(02)00902-X.
1333 Steefel C. I., Druhan J. L. and Maher K. (2014) Modeling coupled chemical and isotopic
1334 equilibration rates. *Procedia Earth Planet. Sci.* **10**, 208–217. Available at:
1335 https://doi.org/10.1016/j.proeps.2014.08.022.
1336 Steefel C. I., Yabusaki S. B. and Mayer K. U. (2015) Reactive transport benchmarks for
1337 subsurface environmental simulation. *Comput. Geosci.* **19**, 439–443. Available at:
1338 https://link.springer.com/article/10.1007/s10596-015-9499-2.
1339 Steinhoefel G., Breuer J., von Blanckenburg F., Horn I. and Sommer M. (2017) The dynamics

of Si cycling during weathering in two small catchments in the Black Forest (Germany) traced by Si isotopes. *Chem. Geol.* **466**, 389–402. Available at: http://www.sciencedirect.com/science/article/pii/S0009254117303844.

Tatzel M., von Blanckenburg F., Oelze M., Schuessler J. A. and Bohrmann G. (2015) The silicon isotope record of early silica diagenesis. *Earth Planet. Sci. Lett.* **428**, 293–303. Available at: https://www.sciencedirect.com/science/article/pii/S0012821X15004458?via%3Dihub.

Tipper E. T., Galy A. and Bickle M. J. (2008) Calcium and magnesium isotope systematics in rivers draining the Himalaya-Tibetan-Plateau region: Lithological or fractionation control? *Geochim. Cosmochim. Acta* **72**, 1057–1075. Available at: http://www.sciencedirect.com/science/article/pii/S0016703707006898.

Tipper E. T., Galy A. and Bickle M. J. (2006) Riverine evidence for a fractionated reservoir of Ca and Mg on the continents: Implications for the oceanic Ca cycle. *Earth Planet. Sci. Lett.* **247**, 267–279. Available at: http://www.sciencedirect.com/science/article/pii/S0012821X06003360.

Tobler D. J., Shaw S. and Benning L. G. (2009) Quantification of initial steps of nucleation and growth of silica nanoparticles: An in-situ SAXS and DLS study. *Geochim. Cosmochim. Acta* **73**, 5377–5393. Available at: http://www.sciencedirect.com/science/article/pii/S0016703709003858.

Urr H. H. D. ¨, Meybeck M., Hartmann J., Laruelle G. G. and Roubeix V. (2011) Global spatial distribution of natural riverine silica inputs to the coastal zone. *Biogeosciences* **8**, 597–620. Available at: www.biogeosciences.net/8/597/2011/.

Walter L. M. and Morse J. W. (1985) The dissolution kinetics of shallow marine carbonates in seawater: A laboratory study. *Geochim. Cosmochim. Acta* **49**, 1503–1513. Available at: https://www.sciencedirect.com/science/article/pii/0016703785902558#bBIB43.

1365 Wiechers H. N. S., Sturrock P. and Marais G. v. R. (1975) Calcium carbonate crystallization
1366 kinetics. *Water Res.* **9**, 835–845. Available at:
1367 http://www.sciencedirect.com/science/article/pii/0043135475901438.
1368 Wiederhold J. G., Kraemer S. M., Teutsch N., Borer P. M., Halliday A. N. and Kretzschmar
1369 R. (2006) Iron Isotope Fractionation during Proton-Promoted, Ligand-Controlled, and
1370 Reductive Dissolution of Goethite. *Environ. Sci. Technol.* **40**, 3787–3793. Available at:
1371 http://dx.doi.org/10.1021/es052228y.
1372 Zhang Y. and Dawe R. (1998) The kinetics of calcite precipitation from a high salinity water.
1373 *Appl. Geochemistry* **13**, 177–184. Available at:
1374 http://www.sciencedirect.com/science/article/pii/S0883292797000619.
1375 Zhu C. and Lu P. (2009) Alkali feldspar dissolution and secondary mineral precipitation in
1376 batch systems: 3. Saturation states of product minerals and reaction paths. *Geochim.*
1377 *Cosmochim. Acta* **73**, 3171–3200. Available at:
1378 https://www.sciencedirect.com/science/article/pii/S0016703709001586?via%3Dihub.
1379 Ziegler K., Chadwick O. A., Brzezinski M. A. and Kelly E. F. (2005) Natural variations of
1380 δ30Si ratios during progressive basalt weathering, Hawaiian Islands. *Geochim.*
1381 *Cosmochim. Acta* **69**, 4597–4610. Available at:
1382 http://www.sciencedirect.com/science/article/pii/S001670370500431X.
1383
1384
1385
1386 **TABLES**

1387 **Table 1.** Initial experimental conditions for all three amorphous silica precipitation batch runs

Physical parameters[*]	**High SA**	**Med SA**	**Low SA**
SiO_2 [mM]	5.3±0.7	5.3±0.4	5.3±0.5
Ω [log Q/K]	0.48±0.06	0.48±0.04	0.48±0.05
$SiO_{2(aq)}$ [g]	0.016±0.002	0.080±0.007	0.080±0.008
$SiO_{2(s)}$ [g]	0.50±0.01	4.00±0.01	4.00±0.01
$SiO_{2(s)}$: $SiO_{2(aq)}$ [g/g][†]	31±4	50±5	50±5

S [m^2]	25±8	0.54±0.02	0.31±0.02

*Error calculations are described in **Table 2**

† solid to fluid mass ratios calculated as the total amount of SiO_2 present in both solid and fluid phase at given time. Error calculated based on standard error propagation.

Table 2. Results of amorphous silica precipitation batch experiments

time	$M_{SiO2(aq)}$[a]	$N_{SiO2(ppt)}$[b]	f[c]	Ω[d]	S[e]	$logR_{bulk}$	$logR_p$	$\delta^{30}Si_{fluid}$	$\delta^{30}Si_{ppt}$[f]	α_{obs}[g]
days	**mM**	**mmoles**		**log (Q/K)**	**m^2**	**mol s^{-1}**	**mol $m^{-2}s^{-1}$**	**‰ ± (2σ) n=3**	**‰ ± (σ)**	
Higher surface area batch, SA = 50 m^2/g, solid:fluid = 31 g $SiO_{2(s)}$ /g $SiO_{2(aq)}$, pH = 7.35, T = 20 ℃										
0.00	5.3±0.7	-	-	0.48±0.06	25±8	-	-	-2.03±0.04	-	-
0.02	5.1±0.5	0.02±0.04	0.002±0.001	0.47±0.04	24±9	-8.09	-9.48	-1.68±0.07	-5.4±1.4	0.9963
0.11	4.6±0.6	0.05±0.04	0.006±0.001	0.42±0.06	24±9	-8.44	-9.82	-1.51±0.05	-4.0±1.0	0.9977
0.19	4.3±0.7	0.07±0.04	0.008±0.001	0.39±0.06	23±9	-8.52	-9.90	-1.34±0.05	-3.7±0.6	0.9979
0.93	3.4±0.9	0.12±0.05	0.01±0.01	0.29±0.08	23±9	-9.15	-10.51	-1.03±0.04	-3.2±0.5	0.9980
1.00	3.3±0.1	0.13±0.04	0.01±0.01	0.28±0.01	22±9	-8.98	-10.33	-1.05±0.04	-3.1±0.5	0.9982
2.00	2.9±0.6	0.15±0.03	0.02±0.01	0.22±0.05	22±9	-9.57	-10.92	-1.19±0.04	-2.6±0.4	0.9987
8.87	2.3±0.2	0.18±0.03	0.02±0.01	0.12±0.01	21±9	-10.32	-11.65	-1.63±0.05	-2.2±0.4	0.9994
13.88	2.2±0.5	0.18±0.02	0.02±0.01	0.10±0.02	21±9	-10.88	-12.20	-2.01±0.05	-2.0±0.3	1.0000
18.95	2.2±0.4	0.19±0.03	0.02±0.01	0.10±0.02	20±9	-11.17	-12.49	-2.25±0.04	-1.9±0.3	1.0003
31.08	2.1±0.4	0.19±0.04	0.02±0.01	0.07±0.02	20±8	-11.17	-12.47	-2.19±0.05	-1.9±0.3	1.0002
Medium surface area batch, SA = 0.127 m^2/g, solid:fluid = 50 g $SiO_{2(s)}$ /g $SiO_{2(aq)}$, pH = 7.31, T = 20 ℃										
0.00	5.3±0.4	-		0.48±0.04	0.54±0.02	-	-	-2.08±0.07	-	-
1.83	4.6±0.4	0.21±0.11	0.003±0.001	0.42±0.04	0.54±0.06	-8.88	-8.62	-1.44±0.12	-5.5±1.7	0.9959
2.90	4.1±0.4	0.32±0.16	0.004±0.001	0.38±0.04	0.53±0.06	-8.90	-8.63	-1.25±0.10	-4.7±1.0	0.9966
4.23	3.7±0.8	0.44±0.15	0.01±0.01	0.33±0.08	0.52±0.06	-8.98	-8.70	-1.11±0.24	-4.5±0.9	0.9963
4.95	3.6±0.5	0.47±0.23	0.01±0.01	0.32±0.04	0.52±0.06	-9.32	-9.04	-0.86±0.09	-3.9±0.7	0.9966
9.00	3.2±0.4	0.58±0.23	0.01±0.01	0.27±0.03	0.51±0.06	-9.52	-9.23	-0.79±0.07	-3.8±0.5	0.9970
14.79	3.1±0.7	0.62±0.15	0.01±0.01	0.25±0.06	0.51±0.06	-10.10	-9.80	-0.75±0.04	-3.6±0.5	0.9971
27.95	2.9±0.6	0.66±0.18	0.01±0.01	0.23±0.05	0.50±0.06	-10.43	-10.13	-0.75±0.11	-3.4±0.5	0.9973
30.00	3.0±0.5	0.66±0.21	0.01±0.01	0.23±0.04	0.49±0.06	-10.40	-10.09	-0.71±0.14	-3.4±0.5	0.9973
Low surface area batch, SA = 0.072 m^2/g, solid: fluid = 50 g $SiO_{2(s)}$ /g $SiO_{2(aq)}$, pH = 7.30, T = 20 ℃										
0.00	5.3±0.5	-		0.48±0.05	0.31±0.02	-	-	-2.14±0.07	-	-
1.83	4.7±0.5	0.17±0.13	0.002±0.001	0.43±0.04	0.31±0.04	-8.98	-8.47	-1.59±0.06	-6.0±1.9	0.9956
2.90	4.4±0.4	0.26±0.17	0.004±0.001	0.41±0.04	0.31±0.04	-9.05	-8.54	-1.44±0.06	-5.2±1.3	0.9962
4.23	4.2±0.6	0.32±0.15	0.004±0.001	0.38±0.06	0.30±0.04	-9.28	-8.76	-1.38±0.06	-4.6±1.1	0.9967
4.95	4.1±0.3	0.35±0.18	0.005±0.001	0.37±0.03	0.30±0.04	-9.22	-8.70	-1.37±0.04	-4.3±0.8	0.9970
9.00	3.9±0.3	0.41±0.17	0.01±0.01	0.35±0.03	0.30±0.04	-9.81	-9.28	-1.24±0.27	-4.2±0.9	0.9970
14.79	3.8±0.4	0.44±0.10	0.01±0.01	0.34±0.04	0.29±0.04	-10.26	-9.72	-1.25±0.08	-4.0±0.7	0.9972
27.95	3.6±0.5	0.49±0.12	0.01±0.01	0.32±0.05	0.29±0.04	-10.30	-9.77	-1.14±0.04	-3.9±0.6	0.9973
30.00	3.6±0.7	0.50±0.16	0.01±0.01	0.32±0.06	0.29±0.04	-10.24	-9.70	-1.18±0.05	-3.8±0.6	0.9974
Am. Silica initial (avg, n=3)									-1.77±0.05	
Am. Silica final (avg, n=3)									-1.81±0.03	

a. measured values with standards errors of 10% for concentrations (1SD) .

b. mass precipitated calculated by subtracting dissolved $SiO_{2(aq)}$ concentrations between time intervals.

Error was propagated according to sum of squares: $\sigma N_{SiO_{2(ppt)}} = \sqrt{\sigma N^2_{SiO_{2(ppt)}\text{-I}} + \sigma N^2_{SiO_{2(ppt)}\text{-II}}}$

c. The fraction of Si in the new precipitate relative to the amorphous silica seed mass (error on weighed seeds ($\sigma_{N_{SiO_2,seed}}$) ± 0.001 g). Error was propagated according to sum of squares: $\sigma_f = \sqrt{\left(\frac{\sigma_{N_{SiO_2(ppt)}}}{N_{SiO_2(ppt)}}\right)^2 + \left(\frac{\sigma_{N_{SiO_2,seed}}}{N_{SiO_2,seed}}\right)^2} \times f$

d. calculated saturation states (log Q/K_{sp}) with standard errors determined through standard error propagation $\sigma_\Omega = \sqrt{\left(\frac{\sigma_{M_{SiO_2aq}}}{M_{SiO_2,aq}}\right)^2} \times \Omega$.

e. volume-corrected surface area using initial BET measured or calculated surface areas, the initial total mass of am.silica present in reactor, and the reactor fluid volume at a given time *t* (**Section 4.1**)

f. silicon isotope composition of mass precipitated calculated using isotope mass balance (**eq. 6**). Associated error calculated based on error propagation (see **Section 3.4**)

g. calculated observed fractionation factors based on ratio of precipitated and fluid phase silicon isotope ratios (**$\delta^{30}Si_{ppt}$** + 1000)/ (**$\delta^{30}Si_{fluid}$** + 1000, **eq.7**).

Table 3. Transient model input parameter values

Input parameters	**High SA**	**Medium SA**	**Low SA**
Duration (days)	35	35	35
Δt (days)	5.0 x 10^{-5}	5.0 x 10^{-5}	5.0 x 10^{-5}
A (timestep average)	20,000	800,000	600,000
log k^a (moles m^{-2} s^{-1})	-9.67	-9.67	-9.67
$SiO_{2(aq)}$ (mM)	5.30	5.30	5.30
pH_{init}	7.35	7.31	7.30
Temperature (°C)	20	20	20
solid:fluid ($m^3_{am.silica}/m^3_{fluid}$)	0.0050	0.0086	0.0087
surface area (m^2/g)	50.0	0.127	0.072
$\delta^{30}Si_{fluid,init}$ (‰)	-2.03	-2.08	-2.14
$\delta^{30}Si_{am.silica}$ (‰)	-1.80	-1.80	-1.80
α_{kin} [b]	0.9967	0.9967	0.9967
α_{eq}	1.0000	1.0000	1.0000

a. Precipitation rate constant value reported by Rimstidt & Barnes (1980) for 20°C
b. Kinetic fractionation factor reported by Roerdink et al. (2015)

Table 4. Fluid interaction depths into amorphous silica

Depth calc. methods	**High SA**	**Medium SA**	**Low SA**
Transient (this study)	0.095 nm	14.3 nm	27.9 nm

Mavromatis et al. (2017)	0.110 nm	22.4 nm	34.1 nm

FIGURE CAPTIONS

Figure 1. Timeseries of (**A**) dissolved silica concentrations and (**B**) corresponding fluid silicon isotope ratios for amorphous silica precipitation experiments conducted at 20°C and pH ~ 7.3. Error bars correspond to 2 standard deviation. High (50 m^2/g), medium (0.127 m^2/g), and low (0.072 m^2/g) surface area experiments are shown here in red circles, green diamonds, and blue squares respectively. High surface area experiments are compared against the Roerdink et al. (2015) study (grey open circles). General fluid $\delta^{30}Si$ trends start at values close to the bulk solid phase composition (grey horizontal line) followed by kinetic enrichment during precipitation and subsequent isotopic re-equilibration, the extent of which appears to be dependent on the surface area.

Figure 2. Conceptual model of transient, isotopic exchange between a mineral and surrounding fluid that is governed by the balance between the forward, precipitation ($\mathbf{R_f}$) and backward, dissolution ($\mathbf{R_b}$) rates. Any imbalance between the forward and backward reaction rates where $\mathbf{R_f} > \mathbf{R_b}$ results in precipitation and kinetic fractionation (**A**). When these two rates become equal to one another (i.e. at dynamic equilibrium) than isotopic fractionation is increasingly influenced by equilibrium behavior as a result of reversible isotopic exchange (**B**). The evolution of the fluid and solid phase isotope ratios are shown under the scenarios of isotopic re-equilibration with (**C**) the bulk solid (volume averaged approach), assuming a steady state surface isotopic composition (DePaolo, 2011) and (**D**) with a growing mineral surface coupled to an isotopically co-evolving fluid phase, resulting in an isotopically zoned solid phase.

Figure 3. Rayleigh model predictions for both fluid (solid black line), instantaneously precipitated amorphous silica (dashed line), and cumulative precipitated amorphous silica (solid yellow line) $\delta^{30}Si$ as a function of the fraction of amorphous silica precipitated (f_{precip}). Experimental results of both measured fluid (filled circles) and calculated cumulative precipitated amorphous silica (open circles) are shown for (A) the Roerdink et al. (2015) study, and the present study (**B**) high, (**C**) medium, and (**D**) low surface area experiments. Cumulatively precipitated $\delta^{30}Si$ were determined through closed system, isotope mass balance calculations. A fixed α_{kin} of 0.9967 was implemented for all Rayleigh predictions. Error bars for fluid $\delta^{30}Si$ and precipitated $\delta^{30}Si$ correspond to 2 standard deviation and 1 standard deviation respectively.

Figure 4. Calculated fractionation factors for amorphous silica precipitation as a function of precipitation rate (**A**) as reported by the Roerdink et al., (2015), (**B**) from our high, (**C**) medium, and (**D**) low surface area experiments. The DePaolo (2011) surface reaction kinetic model is represented as a black line and is based on the relative contributions of α_{kin} (0.9967) and α_{eq} (1.0002) and a dissolution rate, $R_b = 1.95 \times 10^{-11}$ mol m^{-2} s^{-1} (Loucaides et al., 2008). At relatively fast precipitation rates, $\delta^{30}Si$ fractionation is kinetically controlled whereas at slow precipitation rates equilibrium fractionation exerts a stronger influence. In the high surface area case, the considerable variability in the apparent fractionation factor as a function of log R_p reflects mixtures of both α_{kin} and α_{eq}. A narrower range of fractionation is expressed in the medium and low surface area cases. Surface kinetic model results are shown for different α_{kin} values of (**C**) 0.9959 (green dashed line) and (**D**) 0.9956 (blue dashed line), respectively, but these models do not reproduce the remainder of the datasets.

Figure 5. Transient model results for (**A**) aqueous silica concentrations with time during amorphous silica precipitation for the high (red line), medium (green line), and low (blue line) surface area simulations compared against experimental data (filled circles). Corresponding simulations of fluid $\delta^{30}Si$ were run under three different isotopic exchange scenarios between the growing amorphous silica and the surrounding fluid: (**B**) no back reaction allowed (i.e. no isotopic re-equilibration) and $\alpha_{obs} = \alpha_{kin}$ (0.9967); (**C**) fluid isotopic re-equilibration with the bulk solid isotopic composition ($^{i}X_{bulk}$); (**D**) fluid isotopic re-equilibration with a co-evolving mineral surface composition ($^{i}X_{surface}$). Experimental data are shown with error bars represent 2 standard deviation.

Figure 6. Sensitivity analysis of the time interval, T, for the high surface area case. Concentration (**A**) and fluid $\delta^{30}Si$ (**B**) timeseries for both the experimental data (solid red circle, error bars correspond to 2 standard deviation) and transient simulations (solid lines) are shown. Three time interval scenarios are presented that reflect the running average of the isotopic composition of silica mass precipitated over the past (1) 2.4 hrs (light red line), (2) 1 day (red line), and (3) 10 days (dark red line). These three simulations are indistinguishable in the silicon concentrations.

Figure 7. Amorphous silica surface thickness accumulation through time. Surface growth was calculated both experimentally for the high SA (red circle), medium SA (green diamond), and low SA (blue square) cases, and numerically (solid lines) from our transient model simulations shown as solid lines. Results are compared against Geilert et al. (2014) reported values (open circles).

Figure 8. Transient model results of the bulk and cumulative newly precipitated amorphous silica $\delta^{30}Si$ tracked throughout the simulations for the (**A**) high, (**B**) medium, and (**C**) low surface area cases. Experimentally measured $\delta^{30}Si$ (filled circles) and numerically calculated $\delta^{30}Si$ (colored, solid lines) for the fluid phase are presented. Good agreement is found between $\delta^{30}Si_{ppt}$ (shown as grey, open points) calculated from isotope mass balance (error bars correspond to 1 standard deviation, **Table 2**), and numerically estimated accumulated $\delta^{30}Si$ (grey solid lines). Measured bulk $\delta^{30}Si$ (yellow triangles) are presented alongside transient bulk $\delta^{30}Si$ predictions (black solid lines). In the high SA case, $\delta^{30}Si_{ppt}$ mirrors the evolution of fluid $\delta^{30}Si$ with time and ultimately reach near-equivalent values towards the end of the experiment. This observation is in contrast to the medium and low SA cases where both experimental data and numerical simulations retain far from equilibrium isotopic signatures.

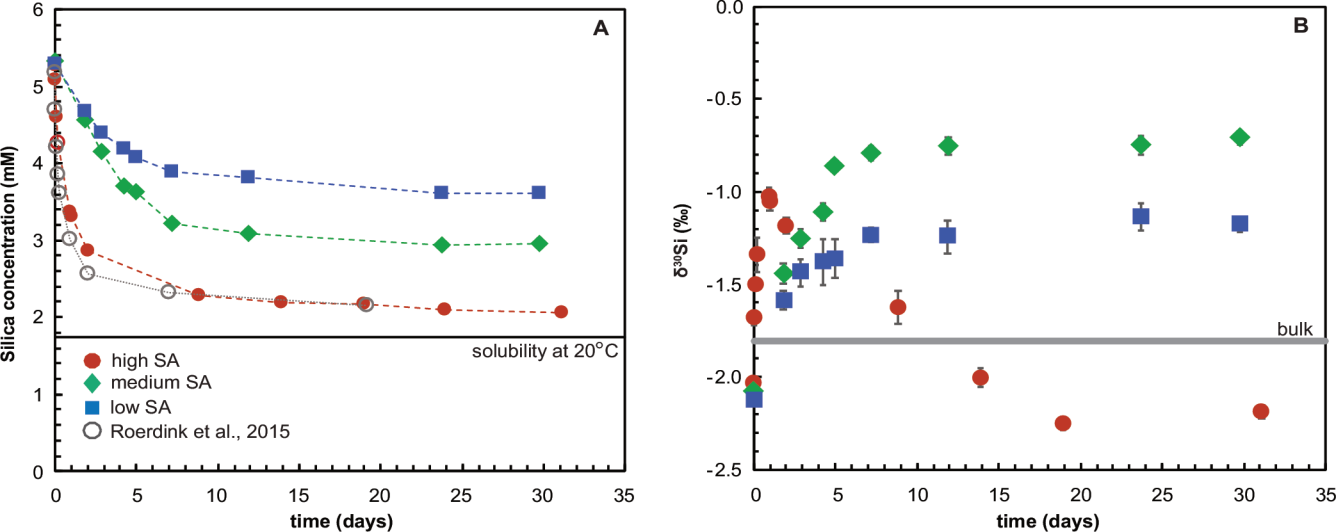
A
B
Silica concentration (mM)
δ30Si (‰)
time (days)
time (days)
solubility at 20°C
high SA
medium SA
low SA
Roerdink et al., 2015
bulk

CONCEPTUAL MODEL OF ISOTOPE BEHAVIOR DURING PRECIPITATION

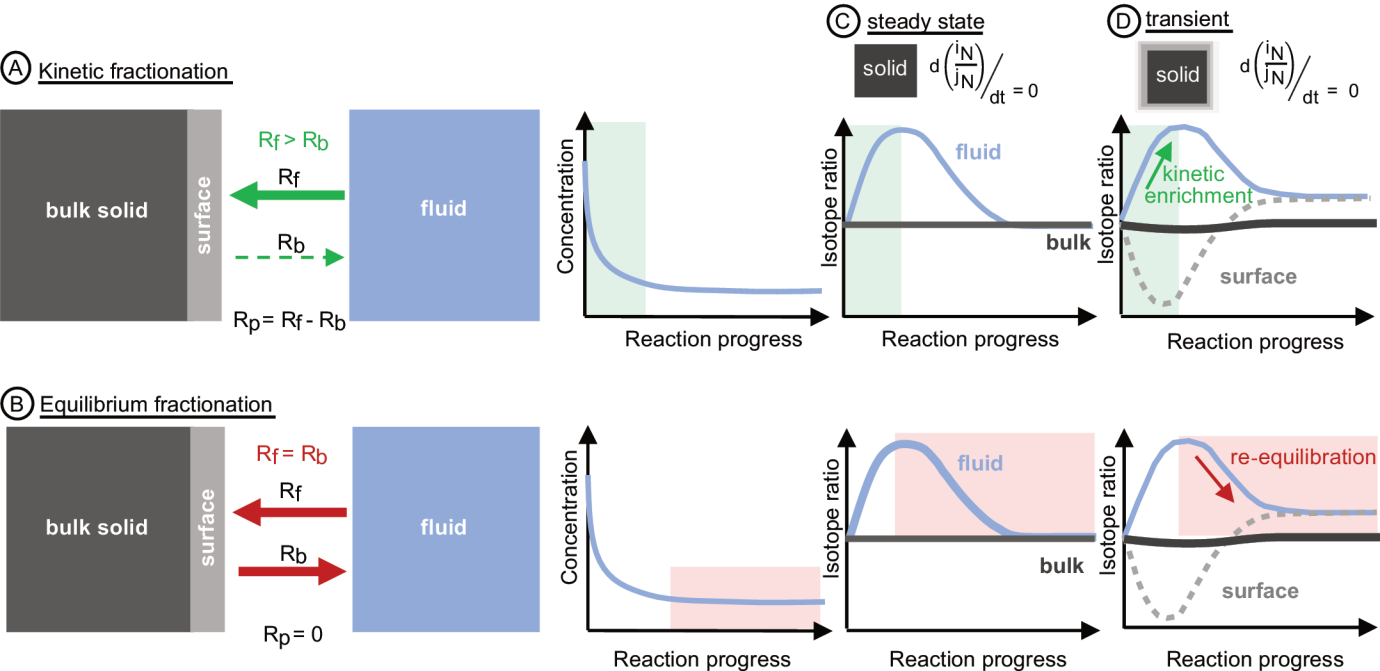

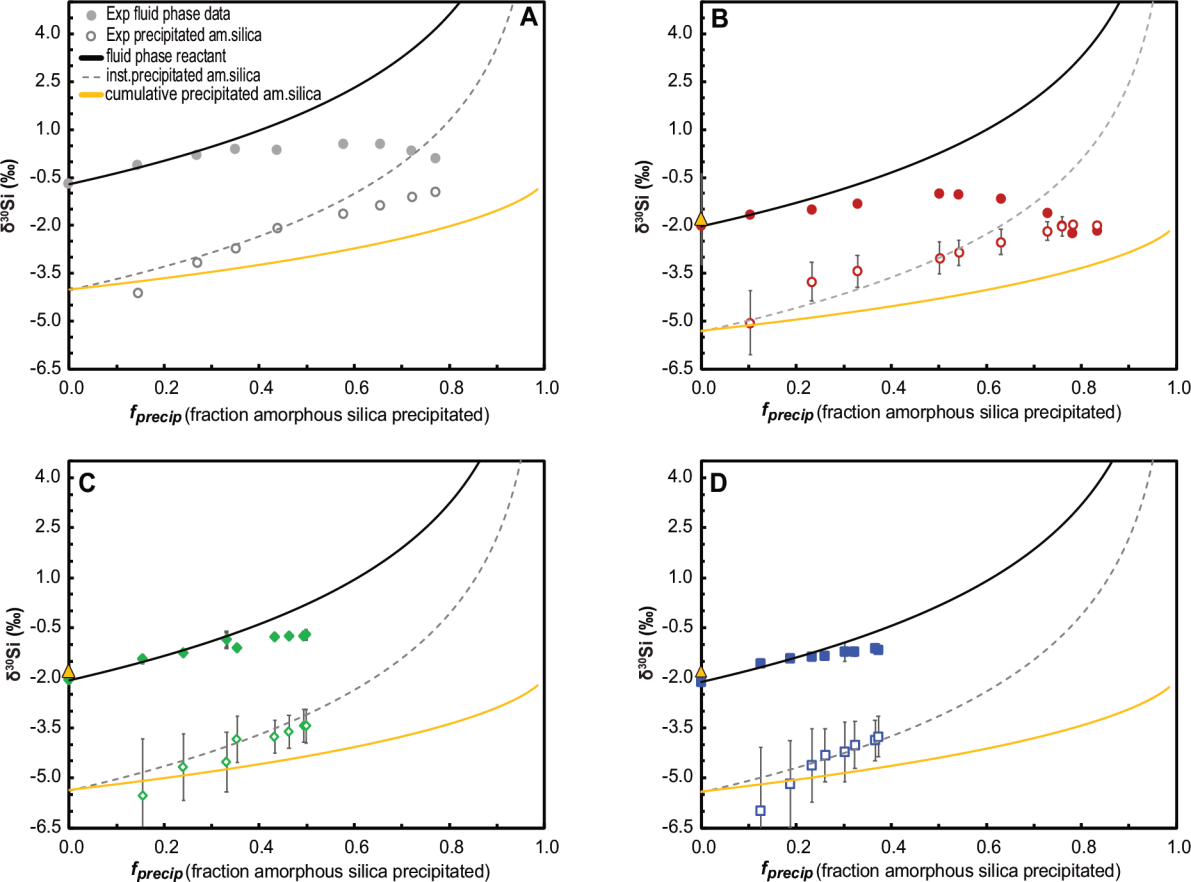
A
B
C
D
Exp fluid phase data
Exp precipitated am.silica
fluid phase reactant
inst.precipitated am.silica
cumulative precipitated am.silica
δ30Si (‰)
fprecip (fraction amorphous silica precipitated)
4.0
2.5
1.0
-0.5
-2.0
-3.5
-5.0
-6.5
0.0
0.2
0.4
0.6
0.8
1.0

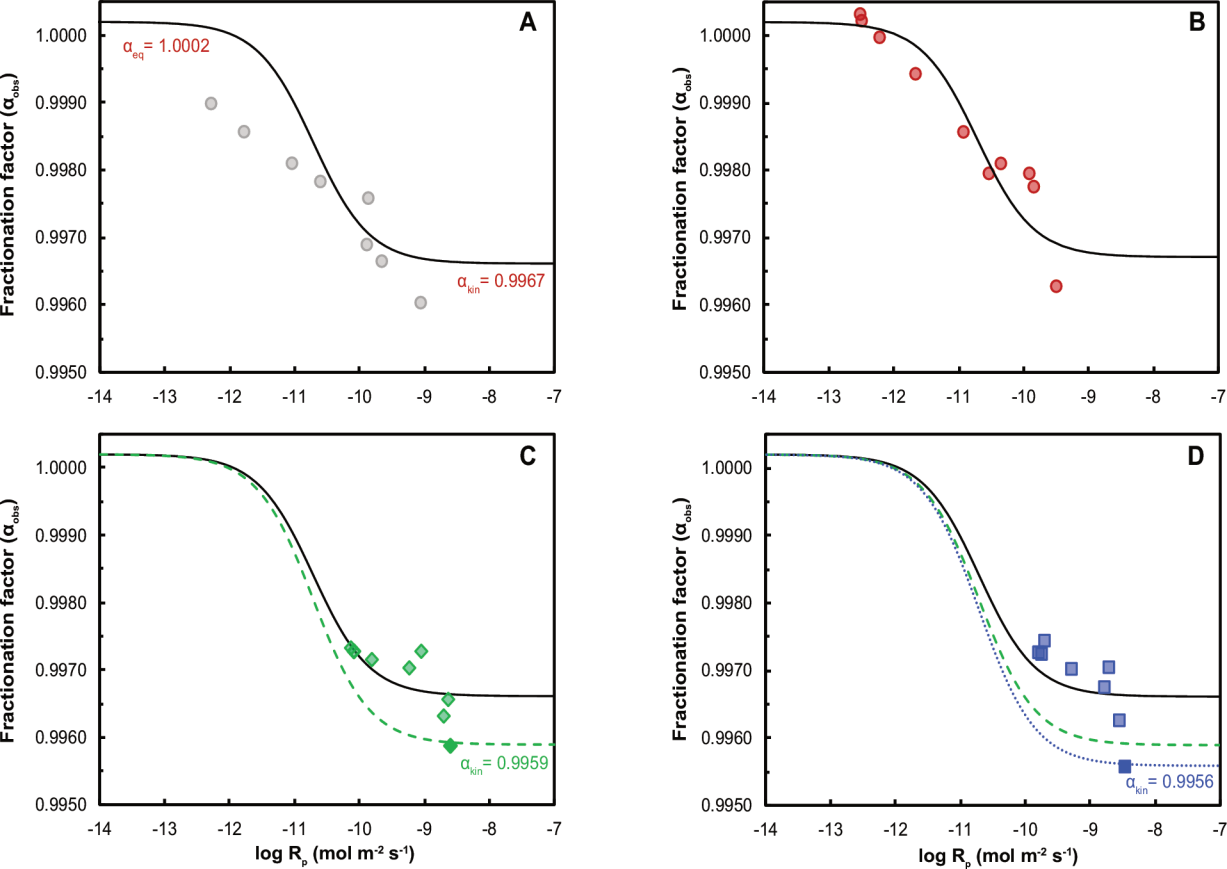
A
α_{eq} = 1.0002
α_{kin} = 0.9967
B
C
α_{kin} = 0.9959
D
α_{kin} = 0.9956
Fractionation factor (α_{obs})
log R_p (mol m^{-2} s^{-1})
1.0000
0.9990
0.9980
0.9970
0.9960
0.9950
-14
-13
-12
-11
-10
-9
-8
-7

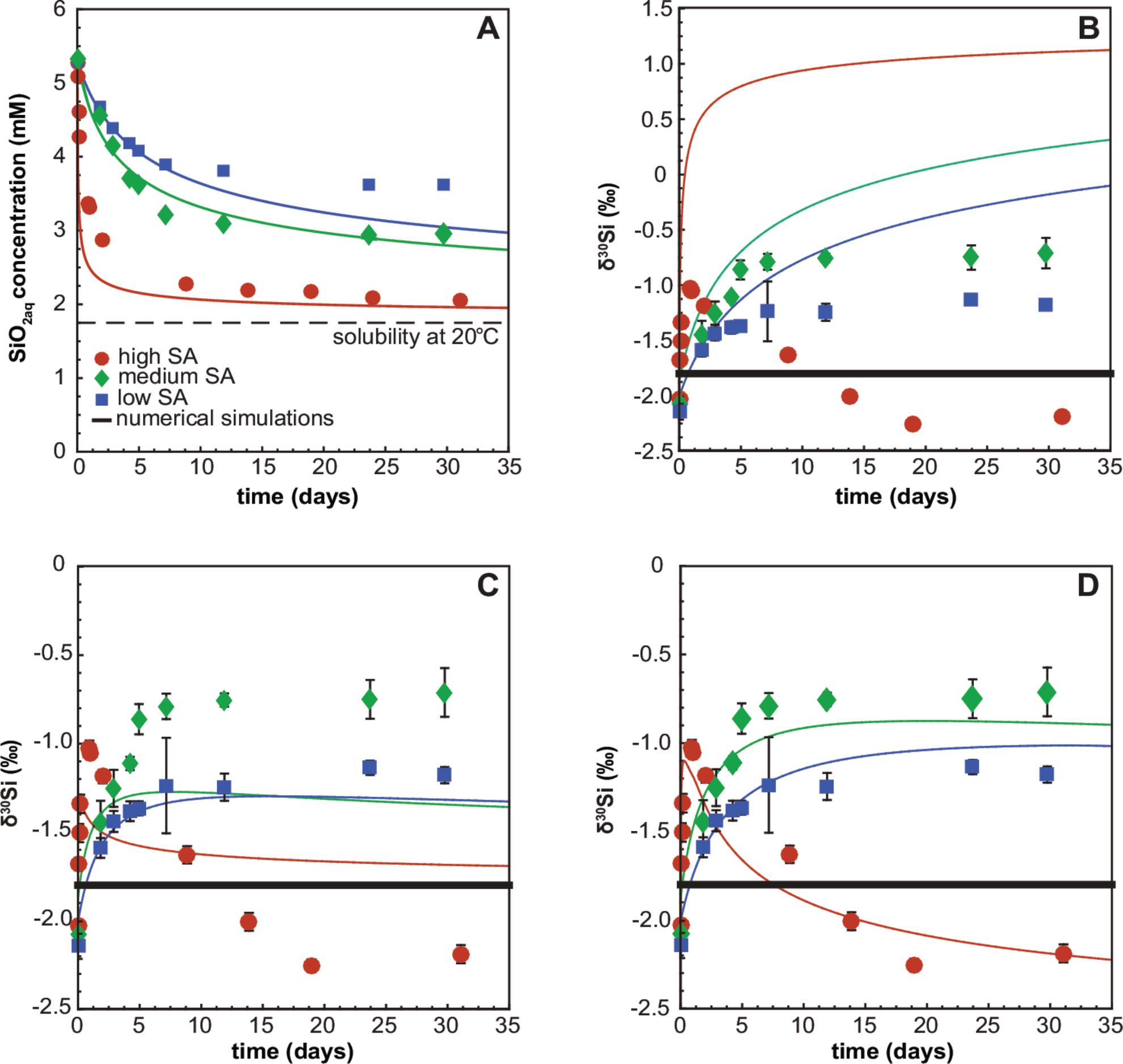
A
B
C
D
SiO_{2aq} concentration (mM)
$\delta^{30}Si$ (‰)
time (days)
solubility at 20°C
high SA
medium SA
low SA
numerical simulations

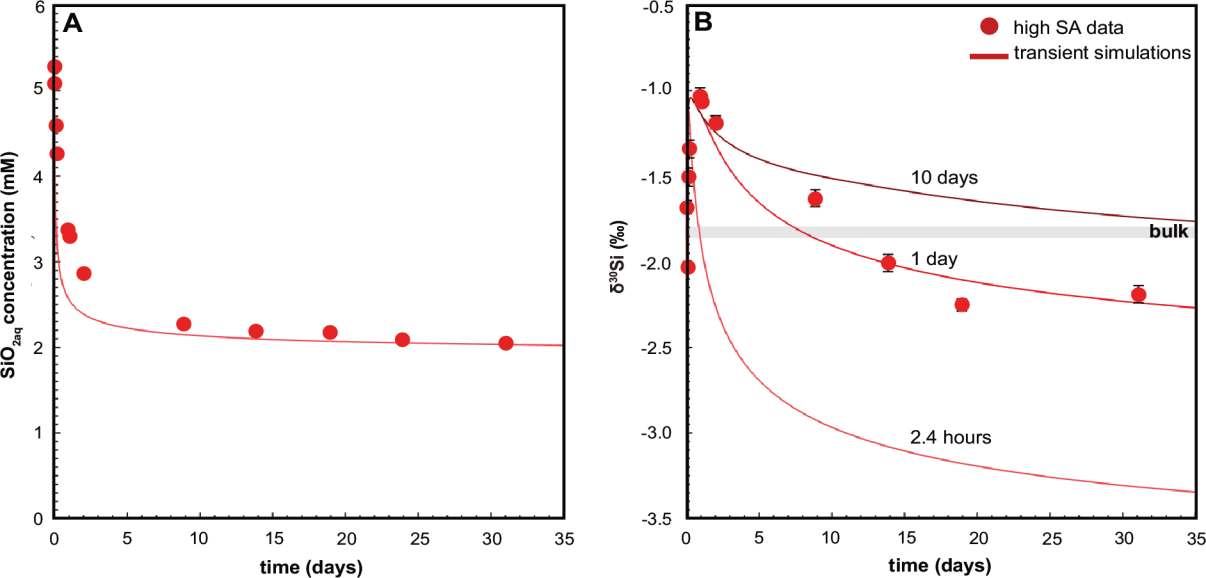
A
SiO2aq concentration (mM)
time (days)
B
high SA data
transient simulations
10 days
bulk
1 day
2.4 hours
δ30Si (‰)
time (days)

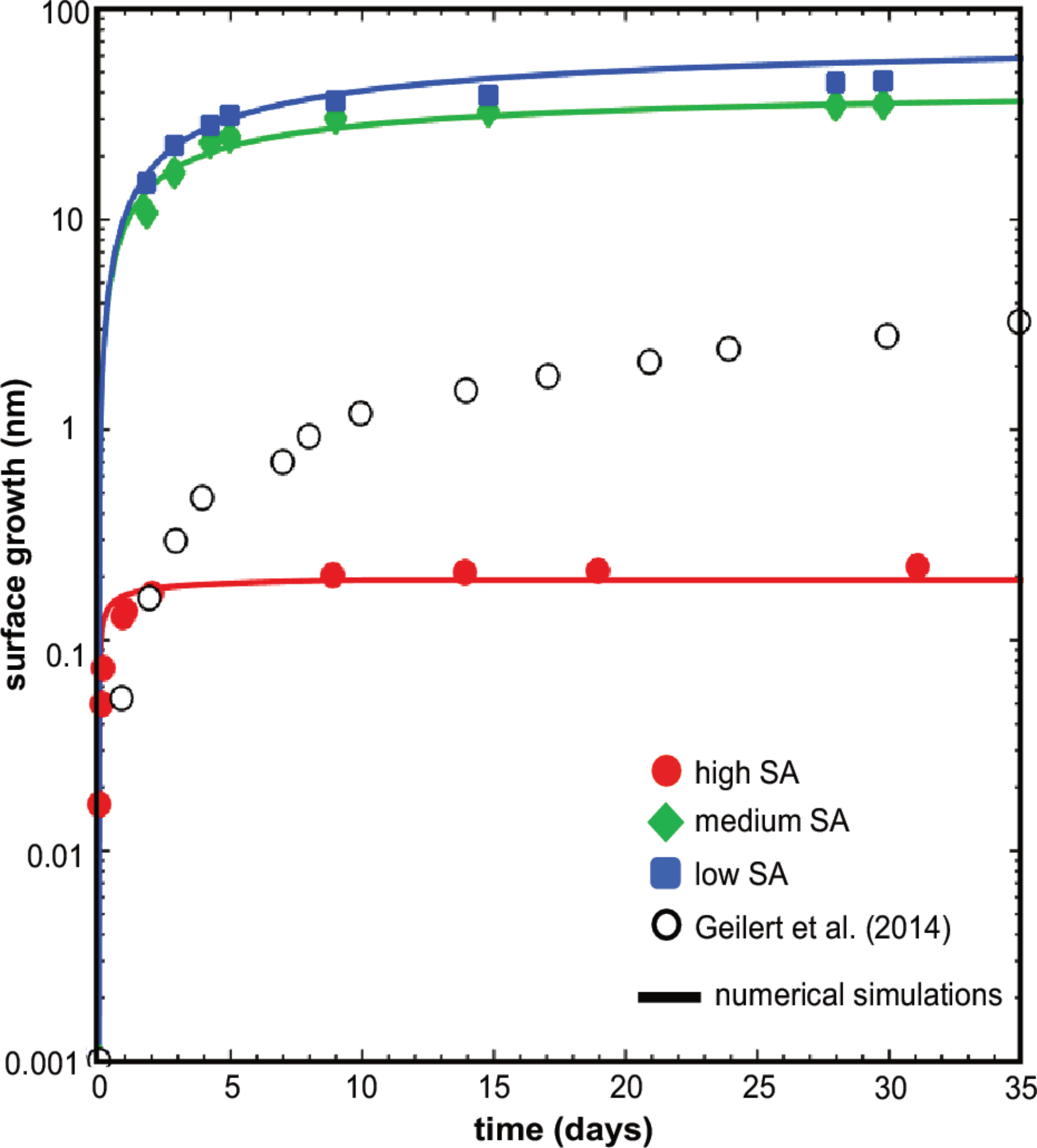
surface growth (nm)
100
10
1
0.1
0.01
0.001
0
5
10
15
20
25
30
35
time (days)
high SA
medium SA
low SA
Geilert et al. (2014)
numerical simulations

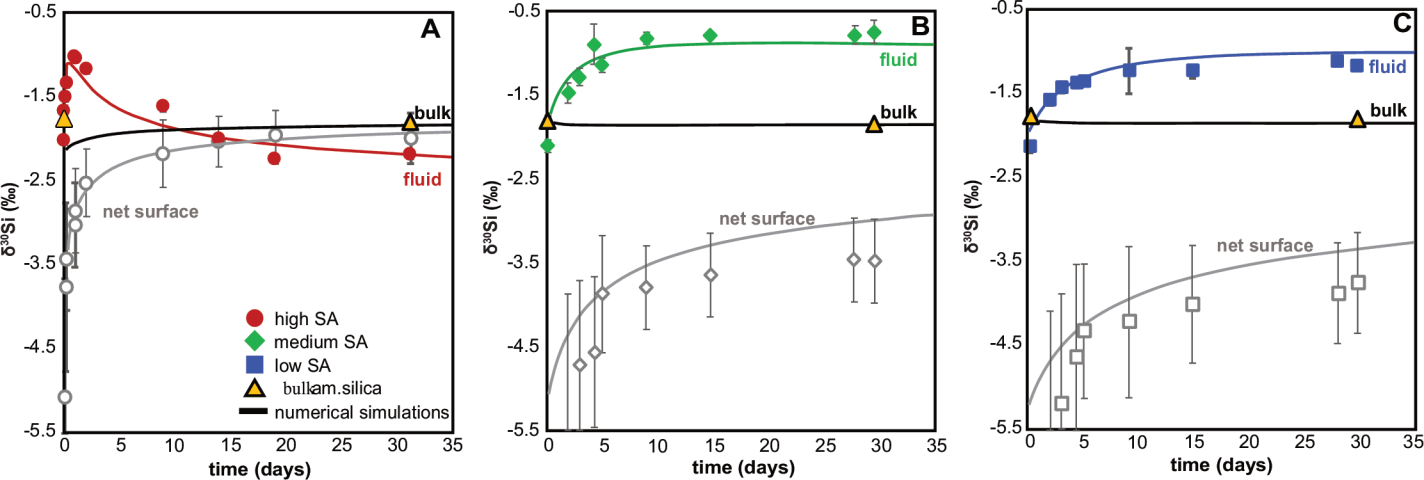
A
B
C
δ30Si (‰)
time (days)
fluid
bulk
net surface
high SA
medium SA
low SA
bulk am.silica
numerical simulations